

# The Physical Origin of the Stellar Initial Mass Function

Hennebelle, P.<sup>1</sup>, Grudić M.<sup>2,3</sup>

<sup>1</sup> Université Paris-Saclay, Université Paris Cité, CEA, CNRS, AIM, 91191, Gif-sur-Yvette, France; email: patrick.hennebelle@cea.fr

<sup>2</sup> Carnegie Observatories, 813 Santa Barbara St, Pasadena, CA 91101, USA, email: mgrudic@carnegiescience.edu

<sup>3</sup> NASA Hubble Fellow

xxxxxx 0000. 00:1–53  
Copyright © 0000 by Annual Reviews.  
All rights reserved

## Keywords

star formation, stellar initial mass function, collapse, gravity, dust, turbulence, magnetic field, stellar feedback

## Abstract

Stars are amongst the most fundamental structures of our Universe. They comprise most of the baryonic and luminous mass of galaxies, synthesise heavy elements, and inject mass, momentum, and energy into the interstellar medium. They are also home to the planets. Since stellar properties are primarily decided by their mass, the so-called stellar initial mass function (IMF) is critical to the structuring of our Universe. We review the various physical processes, and theories which have been put forward as well as the numerical simulations which have been carried out to explain the origin of the stellar initial mass function. Key messages from this review are:

- Gravity and turbulence most likely determine the power-law, high-mass part of the IMF.
- Depending of the Mach number and the density distribution, several regimes are possible, including  $\Gamma_{IMF} \simeq 0, -0.8, -1$  or  $-1.3$  where  $dN/d\log M \propto M^{\Gamma_{IMF}}$ . These regimes are likely universal, however the transition between these regimes is not.
- Protostellar jets can play a regulating influence on the IMF by injecting momentum into collapsing clumps and unbinding gas.
- The peak of the IMF may be a consequence of dust opacity and molecular hydrogen physics at the origin of the first hydrostatic core. This depends weakly on large scale environmental conditions such as radiation, magnetic field, turbulence or metallicity. This likely constitutes one of the reason of the relative universality of the IMF.

## Contents

1. INTRODUCTION .....	2
2. Observational constraints on the IMF .....	3
2.1. Resolved star counts .....	5
2.2. Unresolved populations .....	6
2.3. The core mass function .....	6
3. Physical processes .....	7
3.1. Thermal structure of the cold ISM .....	8
3.2. Supersonic turbulence .....	12
3.3. Gravity, Jeans-instability and gravo-turbulence .....	13
3.4. Ideal and non-ideal MHD .....	15
3.5. Tidal forces and tidal radius .....	17
3.6. Accretion .....	18
3.7. Stellar evolution and feedback .....	19
4. Overview of IMF theories - Success and limit .....	22
4.1. How to explain a broad mass spectrum of stars? .....	22
4.2. How to explain the characteristic mass of stars? .....	29
5. Current state of the art in numerical simulations - testing the theories .....	32
5.1. Numerical algorithms and caveats .....	32
5.2. Barotropic equation of state and hydrodynamical simulations .....	33
5.3. The role of the magnetic field .....	38
5.4. How turbulence and numerical setup influence the IMF .....	39
5.5. Radiative transfer and protostellar heating .....	40
5.6. The influence of metallicity .....	42
5.7. The influence of protostellar jets .....	43
5.8. Massive stellar feedback and cloud disruption .....	44

## 1. INTRODUCTION

In the history of our Universe, stars are playing a fundamental role in many respects. It is now well established that stars are responsible for synthesising the heavy elements such as carbon and oxygen from the primordial hydrogen and helium, which is a necessary step to get molecular complexity and eventually life in the Universe. Low mass stars are also hosting planets providing the necessary source of energy, at least on Earth, to render possible the existence of liquid water during the several Gyrs necessary to develop life. Massive stars on the other hand, exert a considerable influence on the surrounding gas but also at larger galactic scales through both radiation and mechanical energy injections in the interstellar medium (ISM). It is for instance well admitted that massive stars are responsible for setting the amount of galactic UV radiation and to set the star formation efficiency of giant molecular clouds. Finally the light emitted by stars or by ISM constituents such as dust, which have been heated by stars, remains the most important source of information at our disposal to study our Universe.

On the other hand, it is well established that the mass of stars is by far the most important parameters that determine their characteristic and evolution. In this respect the initial stellar mass function (IMF) – the distribution of birth masses of stars – is certainly a fundamental quantity of our Universe. The goal of this review is to present the physical

processes, the theories and the numerical simulations, which have been studied or carried out to understand how the IMF is established. Former reviews on this topic include [Bonnell et al. \(2007\)](#), [Offner et al. \(2014\)](#) and [Lee et al. \(2020\)](#). Several issues and facts are worth stressing and will serve here as a guideline. First of all, the entire known stellar mass range covers about four orders of magnitude, which likely implies that the range of spatial scales involved in the whole star formation process is considerable. This implies that giving the complexity of the baryonic physics, many physical processes are playing an important role in establishing the IMF. Second of all, two remarkable features of the IMF (see figure 1) are the peak it presents around 0.3-0.5  $M_{\odot}$  suggesting the existence of a characteristic mass scale able to imprint the IMF, and the relatively uniform powerlaw exponent that extends over almost 2 decades from about 1 to 100  $M_{\odot}$ . This seemingly suggests the existence of a scale-free regime. Finally, as clearly seen from figure 1, the measured variations of the IMF remains limited, which has sometimes led to the conclusion that the IMF is *universal*. Whereas variations of the IMF seem to be nowadays well established, these variations may still appear limited given the large range of physical conditions in which stars form.

The plan of the review is as follows. In the second part, we briefly discuss the observational constraints that exist on the IMF as well as the analytical descriptions that have been proposed. We also discuss the efforts which have been made to study the dense cores, thought to be the stellar progenitors, and to infer the core mass function (CMF). In the third part we present the physical processes that are relevant for star formation and more precisely which are believed to play a role to establish the IMF. The fourth part is dedicated to the analytical models that have been developed through years to explain the origin of the IMF. We explain the physical ideas and the physical processes that they rely on. We stress their successes and failures. In the fifth part, we describe the numerical simulations which have been carried out to study the IMF, first presenting their finding and then discussing the link they have with the analytical models presented in the fourth section – i.e., do they confirm or invalidate these models? A summary as well as future perspectives conclude the review.

## 2. Observational constraints on the IMF

Historically, most of what is known about the IMF has come from observations ([Bastian et al. 2010](#); [Luhman 2012](#); [Smith 2020](#)). But when discussing IMF measurements it is important to note that the IMF itself is not directly observable, due to the different evolution of high- and low-mass stars. Systems old enough for low-mass stars to be on the main sequence ( $\gtrsim 10$  Myr) are so old that massive stars would have already died. Systems younger than massive star lifetimes may not yet be finished forming stars, and the low-mass, pre-main-sequence stars require additional model assumptions to map their distribution on the Hertzsprung-Russell diagram onto the IMF. Hence inferences about the IMF are necessarily model-dependent, and the modeling uncertainties can be significant (e.g. [Bastian et al. 2010](#)). Apart from this fundamental uncertainty due to stellar evolution, there are many other practical biases and error sources that must be overcome to measure the IMF (e.g. [Kroupa et al. 2013](#); [Hopkins 2018](#)).

An encouraging development in recent decades has been the soundness of the modeling, analysis, and statistical practices used to estimate the IMF. Once common practice, it is increasingly rare for IMF studies to not quote at least some estimate of the statistical error with their measurement. Bayesian techniques that avoid binning and make full use of

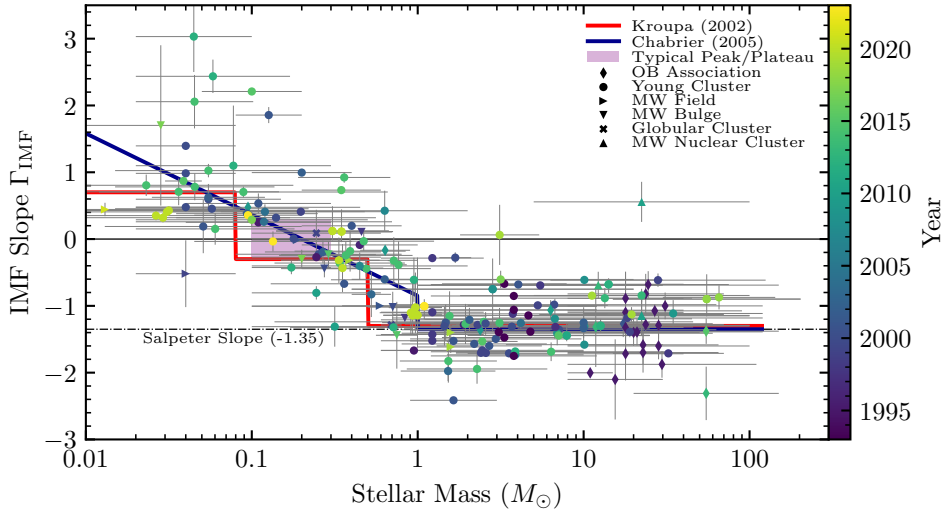


**Figure 1**

IMF slope as a function of the zero-age main sequence stellar mass range over which it is measured by numerous different studies. Horizontal bars give the stellar mass range over which a power-law was fitted; vertical bars plot the  $\pm 1\sigma$  credible region. Note that these data are highly heterogeneous, and the error-bars mostly do not account for systematic errors. [Version with clickable hyperlink points](#). The data compilation and code are available as supplementary material or at [these links](#).

all information are in wider use (e.g. [Weisz et al. 2013](#); [Dib 2014](#)), enabled by advances in computation. It is also increasingly common to use more than one set of model assumptions to assess the impact of systematics, allowing statistical and systematic/modeling errors to be assessed separately (e.g. [Da Rio et al. 2012](#); [Hosek et al. 2019](#)). And the statistics of binary and multiple systems are now better understood ([Moe & Di Stefano 2016](#); [Offner et al. 2022](#)), allowing the effects of unresolved multiplicity to be estimated. These developments have made IMF measurements from recent years generally much easier to interpret critically, although significant modeling uncertainties remain.

A convenient way to parametrize the IMF measured in a certain stellar mass range is to linearize it as a power-law and report the inferred power-law index (the IMF slope  $\Gamma_{IMF}$ ) ([Salpeter 1955](#); [Scalo 1998](#))

$$\frac{dN}{d \log M} \propto MN \propto M^{\Gamma_{IMF}}. \quad 1.$$

With the convention adopted in this review, where the IMF “slope”  $\Gamma_{IMF}$  is the slope in a log-log histogram of stellar masses, the [Salpeter \(1955\)](#) slope is  $\Gamma_{IMF} = -1.35$ . [Figure 1](#) presents a compilation of IMF slopes reported in the literature for numerous different systems in the Local Group (see also [Kroupa 2002](#); [Hillenbrand 2004](#)), for various subintervals across the mass range of stars and sub-stellar objects. For comparison we also plot the two presently most-popular parametrized models ([Kroupa 2002](#); [Chabrier 2003, 2005](#)). Note that Kroupa modeled the IMF as a piecewise function on this diagram, whereas Chabrier modeled the  $< 1M_{\odot}$  range as a log-normal distribution in stellar mass with a slope that varies continuously. Studies comparing these models have generally found them to be

similarly compatible with observations, as well as other parametrizations (Parravano et al. 2011; Maschberger 2013a).

However it is not possible to draw a single curve through all data points in Figure 1 that avoids tension with all measurements; there are many examples of mutually-incompatible slopes measured in similar stellar mass ranges. Due to the many uncertainties, systematic errors are not insignificant, so they certainly account for some of the variation in figure 1 and relieve some of the tension, but not all of it (e.g. Dib 2014). The strong hypothesis of a true IMF universality is unlikely.

Questions of universality aside, the IMF clearly has a remarkable degree of *regularity*: IMF variations may exist, but they are typically not large, at least in nearby galaxies where the IMF can be constrained. At least three fairly robust features are of interest. First, the “peak” of the IMF, which corresponds to the transition between  $\Gamma_{IMF} < 0$  and  $\Gamma_{IMF} > 0$ , is usually found in a fairly narrow mass range of  $\sim 0.1 - 0.3M_{\odot}$ . Second, the range over which the slope varies between -1 and 1 – corresponding to the interval  $[-\sigma^2, \sigma^2]$  for a log-normal form – is about an order of magnitude. Hence the IMF samples a *broad* range of stellar masses, with a log-dispersion  $\sigma \sim 0.5 - 0.6$  dex. And at high masses, the slope tends to be close to the value of -1.35 measured by Salpeter (1955), with relatively little variation in the mass range  $1 - 150M_{\odot}$  except perhaps in the Milky Way nuclear cluster (Bartko et al. 2010; Lu et al. 2013) and some massive starburst clusters (Schneider et al. 2018; Hosek et al. 2019).

There are many different techniques for constraining the IMF, which we outline in the rest of this section, highlighting some significant recent developments.

## 2.1. Resolved star counts

Directly counts of stars of different masses remain a key technique for measuring the IMF within the Local Group, where the necessary resolution is available. Some interesting developments on this front include:

- The Gaia mission has greatly extended the census of stars in the Solar neighborhood with measured spectra, and has provided high-precision parallaxes and proper motions. This permits more-reliable membership assignment for young star clusters in the Solar neighborhood, which can revise the inferred IMF significantly (Luhman 2018). The Milky Way field IMF can now be measured with much larger sample size (Mor et al. 2019; Sollima 2019), down to the brown dwarf and substellar regime (Kirkpatrick et al. 2021). This discipline is now effectively merged with galactic archaeology, because it is at level of precision where the specifics of how the Galaxy assembled and the IMF are tightly entangled. Trends in the IMF with age and metallicity, proposed as far back as (Schmidt 1963), seem to persist under the scrutiny of this greatly-expanded dataset (Li et al. 2023).
- Various measurements in the most massive and dense Local Group clusters have indicated a relatively top-heavy IMF,  $\Gamma_{IMF} \sim -0.8$  (Lim et al. 2013; Pang et al. 2013; Schneider et al. 2018; Hosek et al. 2019). This result, in combination with the well-established top-heavy IMF of the Galactic nuclear cluster (Bartko et al. 2010; Lu et al. 2013), may indicate some connection between the IMF slope and the extreme conditions in which such massive clusters formed. A key caveat does remain: such dense clusters may undergo dynamical evolution over short ( $\lesssim 1$  Myr) timescales. This has two competing effects: mass segregation could make the mass function sampled

in a limited field look top-heavy (Pang et al. 2013), but the preferential ejection of massive stars should also steepen the observed mass function over time (Banerjee & Kroupa 2012).

- The PHAT HST survey of the disk of M31 has produced a large, homogeneous catalogue of young, resolved star clusters, allowing Weisz et al. (2015) to make the most precise measurement of the  $\gtrsim 2 M_{\odot}$  IMF slope to date:  $\Gamma_{IMF} = -1.45^{+0.03}_{-0.06}$ . The posterior on the modeled intrinsic dispersion  $\sigma_{\Gamma}$  is consistent with 0, i.e. there is no strong evidence of major cluster-to-cluster variation, or random systematic errors. This is an important development because observations available in the Milky Way are subject to greater uncertainties in reddening, membership, etc, and it is difficult to distinguish between true intrinsic IMF variation and systematic effects (Massey 2003).
- It is now possible to use large grids of N-body simulations to constrain the overall IMF in globular clusters, with general preference for an IMF that is bottom-light, but with a normal high-mass slope  $\Gamma_{IMF} \sim -1.3$  (Baumgardt & Sollima 2017; Ebrahimi et al. 2020; Baumgardt et al. 2023). The formation process, initial conditions, initial multiplicity properties, binary stellar evolution, and evolution in a galactic context all have major uncertainties, so the model dependence of such measurements should be assessed carefully.

## 2.2. Unresolved populations

Studying the IMF unresolved populations is inherently harder and must rely on careful modeling where several properties of the observed stellar population are degenerate with each other. However, they allow us to probe more extreme regions of the SF parameter space than that in the Local Group.

- Efforts to constrain the low-mass IMF in massive early-type galaxies (Smith 2020) via high-resolution spectral modeling (e.g. van Dokkum & Conroy 2010) have continued, and the trend toward greater mass-to-light ratios (i.e. a steeper  $\approx 0.3 - 0.8 M_{\odot}$  slope) in the central regions of more-massive galaxies persists (Newman et al. 2017; Gu et al. 2022). Gu et al. (2022) documents correlations between the mass-to-light ratio and galactic properties such as velocity dispersion, [Mg/Fe], and [Fe/H].
- The Optical Gravitational Lensing Experiment (OGLE) has provided constraints on the low-mass ( $\sim 0.01 - 0.5 M_{\odot}$ ) IMF in the Galactic bulge/bar region. Wegg et al. (2017) found the IMF to be consistent with the standard IMFs measured in the local field. Chabrier & Lenoble (2023) found that these data specifically prefer the Chabrier (2005) parameters for the log-normal parameterization over those of Chabrier (2003), that this parametrization is preferred over the Kroupa (2002) broken power-law, and that the central region may be bottom-heavy.

## 2.3. The core mass function

Prestellar dense cores (Motte et al. 1998; Ward-Thompson et al. 2007; Könyves et al. 2015), often observed in the continuum, are believed to be the progenitors of stars. That is to say they may constitute the very final coherent gaseous reservoir out of which stars build their masses. This opens the possibility that their mass distribution, the CMF, may be at the origin of the IMF. For this to be true, the correspondance between this material and the

final stellar mass, must be sufficiently good and to a large extent, assessing this remains a challenge (Pelkonen et al. 2021). In particular, defining core boundaries is a complex question moreover since stars are generally found in multiple systems, cores likely lead to the formation of several objects. One of the main arguments in favor of the importance of cores in determining the shape of the IMF has been their relatively similar shapes (e.g. see Figure 16 of Könyves et al. 2015) as inferred for instance in the Herschel Gould Belt survey (André et al. 2010). Both present a powerlaw or lognormal shape at high mass and a peak around  $0.3 M_{\odot}$  for the IMF and  $0.5\text{-}1 M_{\odot}$  for the CMF. The powerlaw of the high mass part inferred for the CMF appears to be compatible or close to the value  $\Gamma_{IMF}$  usually measured for the IMF.

Several studies have questioned the universality of this result. In recent observations, the CMF have been inferred in the active star-formation region W43-MM1 and W43-MM2&MM3 (Motte et al. 2018; Pouteau et al. 2022) and it has been found that the exponent of the powerlaw is significantly flatter than  $\Gamma_{IMF} \simeq -1.3$  with typical values around  $-0.9$  to  $-0.95$  (see however Padoan et al. 2023, for possible biases). Interestingly, as mentioned above, shallower values of  $\Gamma_{IMF}$  have also been inferred in massive and dense local stellar clusters (e.g. Hosek et al. 2019) suggesting a possible common origin.

Second of all, the reliability of the peak of the CMF has been investigated by Louvet et al. (2021) where the cores have been extracted from observational and simulation data smoothed at various spatial resolutions. It has been found that the identified cores strongly vary with resolution and in particular that the peak of the CMF shifts to higher masses as the spatial resolution is reduced. This result questions the existence of a clear resolution independent core definition as well as the existence of a CMF peak. It suggests that the peak of the CMF estimated from the Herschel Gould Belt survey may be overestimated. Interestingly, it has been recently suggested that the mass function of bound cores (seen in C18O) in Orion may present a peak around  $0.1 M_{\odot}$  (Takemura et al. 2023).

To conclude, whereas the correspondance between the CMF and the IMF needs to be further investigated, the cores certainly contribute to the star formation process and as such models of star formation studying the IMF should be able to reproduce the CMF as it certainly constrains the gas physical properties.

### 3. Physical processes

In this section we review the various physical processes that are relevant in the context of the star formation process and the establishment of the IMF. We proceed broadly in *chronological* order, that is to say discussing the processes in the sequential order with which they become relevant. All the discussed topics are complex phenomena which request lengthy developments that are beyond the scope of the present review where only the most important aspects for the origin of the IMF are considered. Complementary information can be found for instance in the recent review by Girichidis et al. (2020). The equations that are generally employed to perform theoretical studies of star formation are the usual fluid equations that apply to a self-gravitating, radiative and magnetized gas. They can be found for instance in Commerçon et al. (2011); Krumholz et al. (2012); Tomida et al. (2013).

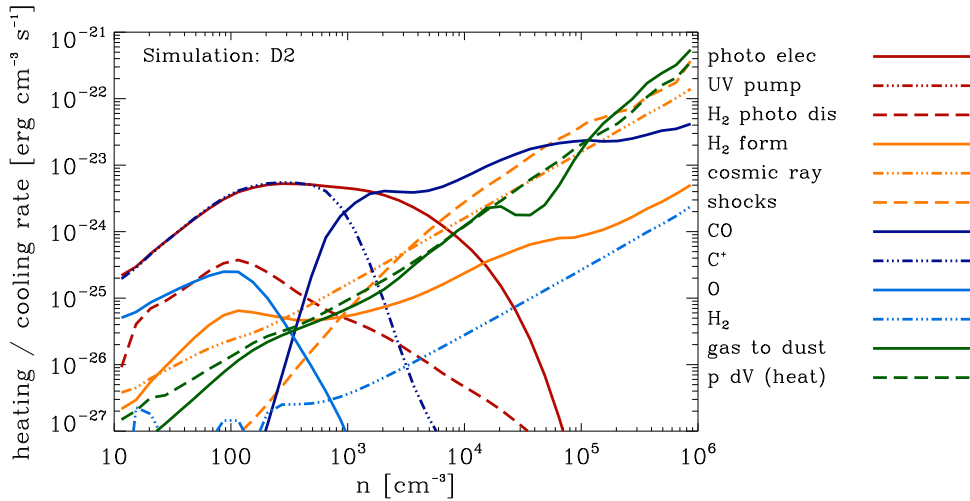


**Figure 2**

Heating and cooling rates of different physical processes as a function of density in a Smoothed Particle Hydrodynamics simulation of a  $10^4 M_{\odot}$  giant molecular cloud with radius 6pc, with composition typical of a Solar neighborhood molecular cloud. Reproduced with permission from [Glover & Clark \(2012\)](#); see their figure 8 for full details.

### 3.1. Thermal structure of the cold ISM

Stars form in the cold, molecular phase of the ISM, where cooling times are generally shorter than other dynamical timescales, so the temperature  $T$  is determined mainly by the balance of heating and cooling processes. This temperature may be important for the IMF because it determines e.g. the Mach number of turbulence and all resulting density statistics, and the Jeans mass at a given density. There are multiple heating and cooling processes that scale steeply with  $T$ , limiting the overall degree of temperature variation. Therefore, the star-forming ISM is often approximated as isothermal, e.g. at  $\sim 10\text{K}$  in conditions found in the Solar neighborhood. This can be a useful approximation, but for the purposes of IMF theory it is important to note that the temperature *will* generally vary with the gas density and chemical composition, the properties and abundance of dust, and the intensity and spectral energy distributions of photons and cosmic rays. The thermal balance of the ISM is a complex and extensive subject addressed by various dedicated texts, e.g. [Tielens \(2005\)](#); [Osterbrock & Ferland \(2006\)](#); [Draine \(2011\)](#).

The situation in Solar neighborhood conditions is summarized in Figure 2 from [Glover & Clark \(2012\)](#), which plots the volumetric heating and cooling rates of the various processes active in a GMC as a function of density. Table 1 lists some of the key processes determining the thermal structure of the cold, star-forming ISM, and the densities at which different processes are important (again, in Solar neighbourhood conditions). The temperature of the cold ISM up to moderate ( $\sim 10^4 \text{cm}^{-3}$ ) densities is determined by heating from the grain photoelectric effect, cosmic rays, and turbulent dissipation, and cooling from  $\text{C}^+$  fine-structure and CO rotational transitions. This shapes the decrease in temperature from a few 100K at  $n_{\text{H}} \sim 10 \text{cm}^{-3}$  to 10 – 20K at  $10^4 \text{cm}^{-3}$ , which will affect the turbulent



Process	Relevant $n_{\text{H}}$ at $Z_{\odot}$	Key species	Rate per H	Refs.
Photoelectric heating	$10^{-2}$ - $10^4 \text{ cm}^{-3}$	Grains, FUV	$\propto Z_{\text{d}} G_0$	1,2,3
Cosmic ray heating	$10^{-2}$ - $10^4 \text{ cm}^{-3}$	Cosmic rays, H, $\text{H}_2$	$\propto \xi_{\text{CR}} f_{\text{atten}}(N_{\text{H}})$	4,5,6
Gravitational PdV work	$10^5 + \text{cm}^{-3}$	Gas	$\propto n_{\text{H}}^{1/2} T$	7,8,9
Turbulent dissipation	$10^2 - 10^6 \text{ cm}^{-3}$	Gas	$\propto \sigma^3/l$	10
$\text{C}^+$ fine structure	$1 - 10^3 \text{ cm}^{-3}$	$\text{C}^+$ , H, $\text{H}_2$	$\propto Z_{\text{C}} \exp(-91/T) n_{\text{H}}$	3,11
C, O fine structure	$1 - 10^2 \text{ cm}^{-3}$	C, O, H, $\text{H}_2$	See refs.	3,14
CO rot. lines (thin)	$10^2 - 10^3 \text{ cm}^{-3}$	CO, $\text{H}_2$	$\propto Z_{\text{C}} n_{\text{H}} T^{3/2}$	12,13
CO rot. lines (thick)	$10^3 - 10^4 \text{ cm}^{-3}$	CO, $\text{H}_2$	$\propto \ \nabla \mathbf{v}\  n_{\text{H}}^{-1} T^4$	12,13
$\text{H}_2$ transitions	None (at $Z_{\odot}$ )	$\text{H}_2$ , HD	See refs.	14,15
Dust-gas collisions	$10^4 + \text{cm}^{-3}$	Gas, grains	$\propto Z_{\text{d}} n_{\text{H}} T^{3/2} (T - T_{\text{d}})$	16,17,18

**Table 1** Summary of processes determining the thermal structure of the cold ISM relevant to fragmentation and the IMF. For each process we give the estimated range of densities at which the process is important in Solar neighborhood ambient conditions, the scaling law for the rate per H nucleus, and useful references for detailed formulae. Note that the density range in which different processes dominate will generally vary with metallicity and radiation field.  $\text{H}_2$  transitions are unimportant at  $Z_{\odot}$ , but are the main coolant at  $\lesssim 10^{-2} Z_{\odot}$  until dust coupling is efficient.  $T$ ,  $T_{\text{d}}$ : gas and dust temperatures,  $G_0$ : FUV radiation field,  $\xi_{\text{CR}}$ : cosmic ray ionization rate,  $f_{\text{atten}}$ : cosmic ray attenuation factor,  $\alpha_{\text{turb}}$ : GMC turbulent virial parameter,  $\sigma$ : ISM velocity dispersion,  $l$ : Scale at which  $\sigma$  is defined,  $Z_i$ : relative mass fraction of species  $i$ . 1: Bakes & Tielens (1994), 2: Weingartner & Draine (2001), 3: Draine (2011), 4: Indriolo & McCall (2012), 5: Neufeld & Wolfire (2017), 6: Padovani (2023). 7: Low & Lynden-Bell (1976) 8: Masunaga et al. (1998) 9: Grudić & Hopkins (2023) 10: (Mac Low 1999) 11: Wiesenfeld & Goldsmith (2014), 12: Gong et al. (2017), 13: Whitworth & Jaffa (2018), 14: Glover & Jappsen (2007) 15: Glover & Abel (2008), 16: Hollenbach & McKee (1979), 17: Goldsmith (2001), 18: Krumholz et al. (2011).

density statistics that are important for gravo-turbulent IMF models. At higher densities, gas cooling due to gas-grain coupling becomes increasingly important, and  $T$  approaches the dust temperature  $T_{\text{d}}$ .

At lower metallicity the hierarchy of different heating/cooling processes can be different. CO cooling is never significant at  $\lesssim 10^{-2} Z_{\odot}$  due to the lesser shielding and maximum abundance. The dust-coupled phase at low metallicity also occurs at higher density, roughly  $n \propto Z_{\text{d}}^{-1}$ . Due to the overall lack of coolants and dust shielding, the equilibrium temperature will generally be significantly higher at low  $Z$ : state-of-the-art thermochemical MHD models typically find a typical factor of  $\sim 2-3$  increase in  $T$  at fixed  $n_{\text{H}}$  going from Solar conditions to  $10^{-2} Z_{\odot}$  (Bialy & Sternberg 2019; Guszejnov et al. 2022; Kim et al. 2023). This implies that the Jeans mass at a given density or pressure will be greater at low  $Z$ , potentially affecting fragmentation. At very low metallicity ( $\lesssim 10^{-3} - 10^{-5} Z_{\odot}$ ) there will be effectively no dust-coupled phase at all, and  $\text{H}_2$  is the only effective low-temperature coolant (Sharda & Krumholz 2022). The first stars would have formed in this dust-free regime, and the inevitably-higher temperature and Jeans mass naturally results in a more top-heavy IMF (Klessen & Glover 2023).

**3.1.1. Dust-coupled regime.** At sufficiently high density and dust abundance,  $T \sim T_{\text{d}}$ , dust-gas collisions become so frequent that the temperature is determined by the balance of dust

cooling ( $\propto \kappa T^4$ ,  $\kappa \propto T^\beta$ ,  $\beta \sim 1 - 2$ ) with radiative or mechanical heating, and the overall temperature evolution can be determined by patching together the various asymptotic regimes (Grudić & Hopkins 2023). If absorption of IR radiation by dust is the main heat source, then the gas will remain essentially isothermal at a certain radiative equilibrium temperature:

$$T_{\text{abs}} = \left( \frac{T_{\text{IR}}^\beta u_{\text{IR}}}{a} \right)^{\frac{1}{4+\beta}} \approx 7\text{K} \left( \frac{T_{\text{IR}}}{20\text{K}} \right)^{\frac{1}{3}} \left( \frac{u_{\text{IR}}}{1\text{eV cm}^{-3}} \right)^{\frac{1}{6}}, \quad 2.$$

where  $T_{\text{IR}}$  is the effective blackbody temperature of the incident IR SED,  $\beta \sim 1 - 2$  is the power-law scaling exponent of the dust opacity law  $\kappa \propto T^\beta$ , and  $u_{\text{IR}}$  is the radiation energy density. The galactic background, reprocessed emission powered by incident light absorbed in the outer parts of the cloud, and emission from nearby protostars can all contribute to the radiation field (Section 3.7.3). If  $PdV$  work due to gravitational collapse dominates over radiative heating, then the balance of heating and cooling gives

$$T_{\text{PdV}} \approx 8\text{K} \left( \frac{C_{\text{ff}}}{Z_{\text{d}}} \right)^{\frac{1}{3+\beta}} \left( \frac{n_{\text{H}}}{10^{10}\text{cm}^{-3}} \right)^{\frac{1}{2(3+\beta)}}, \quad 3.$$

where  $Z_{\text{d}}$  is the mass fraction of dust scaled relative to the Solar neighborhood, and  $C_{\text{ff}} \sim 1$  encodes the rate of collapse relative to freefall (Masunaga et al. 1998). Note that for  $\beta \sim 1 - 2$  this implies that  $T \propto n_{\text{H}}^{\frac{1}{8}} - n_{\text{H}}^{\frac{1}{10}}$ , i.e. nearly but not exactly isothermal.

**3.1.2. Opacity limit density and minimum Jeans mass.** Once the rate of  $PdV$  work exceeds the maximum rate of radiative diffusion of cooling radiation from the collapsing core, the gas can no longer collapse quasi-isothermally. Instead, cooling becomes inefficient and the gas will evolve almost adiabatically; this transition in thermodynamic evolution is known as the opacity limit (Low & Lynden-Bell 1976; Rees 1976; Silk 1977). Let us stress that such high densities are not met in the ISM except in collapsing regions. The density of the adiabatic transition  $n_{\text{ad}}$  depends mainly on dust opacity and the local radiation energy density (Masunaga et al. 1998; Vaytet & Haugbølle 2017; Grudić & Hopkins 2023):

$$n_{\text{ad}} \approx 5.7 \times 10^{10} \text{cm}^{-3} \times \min \left( Z_{\text{d}}^{-\frac{10}{4\beta+7}}, Z_{\text{d}}^{-2/3} (u_{\text{rad}}/100 \text{eV cm}^{-3})^{\frac{2-\beta}{6}} \right), \quad 4.$$

where  $Z_{\text{d}}$  is the Solar-scaled dust opacity parameter<sup>1</sup> and  $u_{\text{rad}}$  is the local radiation energy density; this density is mainly sensitive to  $Z_{\text{d}}$ , so the opacity limit occurs at higher density in low-dust conditions. This expression approximates the transition between the radiation-dominated and mechanical heating-dominated regimes.

The minimum Jeans mass reached at  $\sim n_{\text{ad}}$  is then (Grudić & Hopkins 2023):

$$M_{\text{J,min}} \approx 2 \times 10^{-3} M_{\odot} \max \left( Z_{\text{d}}^{-\frac{1}{4\beta+7}}, Z_{\text{d}}^{1/3} (u_{\text{rad}}/100 \text{eV cm}^{-3})^{\frac{2\beta+5}{24}} \right). \quad 5.$$

Hence, if the radiation field is weak or dust is scarce, the minimum Jeans mass is extremely robust to metallicity and dust properties, varying by at most a factor of  $\sim 3$  over the range

---

<sup>1</sup>Specifically, in our parametrization  $Z_{\text{d}} = \sigma_{\text{d}}(10\text{K})/\sigma_0$  where  $\sigma_{\text{d}}(T_{\text{d}})$  is the Planck-mean dust emission cross section per H nucleus at dust temperature  $T_{\text{d}}$ , and  $\sigma_0 = 4 \times 10^{-26} \text{cm}^2 \text{H}^{-1}$  is a fiducial value typical of widely-used dust models.

$\beta \sim 1-2$  and  $Z_d \sim 10^{-4}-1$ .  $M_{J,\min}$  only scales more steeply with environmental conditions in the radiation-dominated regime, in which  $M_{J,\min} \propto Z_d^{1/3} u_{\text{rad}}^{\frac{2\beta+5}{24}}$ ; this would apply mainly to dust-rich, radiation-dense environments.

The existence of a minimum Jeans mass has led to the idea that this represents the mass of the smallest objects that may form under the influence of gravity and thus this may explain for instance the mass of the brown dwarfs. This argument should be considered with care because when a fragment forms, this leads to the formation of a thermally supported core, as explained below and collapse does not proceed immediately.

**3.1.3. First hydrostatic core and second collapse.** As expressed above,  $M_{J,\min}$  is the smallest self-gravitating mass of gas that is linearly unstable. As the opacity limit is crossed, a quasi-hydrostatic structure is formed (Larson 1969; Masunaga & Inutsuka 2000; Vaytet & Haugbølle 2017): the first hydrostatic core (FHSC) also called the first Larson core. In order for the FHSC to collapse promptly to protostellar density a fragment must become somewhat more massive, so that its central temperature exceeds  $T_{\text{dis}} \sim 1500\text{K}$ , triggering a runaway collapse as energy goes into dissociating  $\text{H}_2$ . Indeed the dissociation of the  $\text{H}_2$  molecule requires about 4.5 eV which corresponds to the thermal energy of a gas at several thousands of Kelvin degrees. This is considerable and it constitutes a very substantial source of cooling that is able to maintain the temperature nearly constant and around  $T_{\text{dis}}$  (with an effective adiabatic index  $\Gamma_{ad} \simeq 1.1$ ) during the second collapse and up to the formation of the second hydrostatic core. To properly describe the gas evolution at these densities, it is necessary to take into account the translational, rotational and vibrational degrees of freedom of molecular hydrogen as well as to include the dissociation of molecular hydrogen, and the ionizations of hydrogen and helium (Black & Bodenheimer 1975; Saumon et al. 1995; Tomida et al. 2013). Note that there are still significant uncertainties due to the unknown  $\text{H}_2$  ortho:para ratio (Vaytet et al. 2014) and dust properties in collapsing cores (Guillet et al. 2020; Lebreuilly et al. 2023b).

Assuming the evolution past  $n_{\text{ad}}$  is isentropic, and that the adiabatic index of  $\text{H}_2$  transitions from  $\gamma_1 = 5/3$  to  $\gamma_2 = 7/5$  at  $T_{\text{ex}} \sim 150\text{K}$  (Vaytet & Haugbølle 2017; Hennebelle et al. 2019), the minimum mass that can undergo second collapse, is

$$\begin{aligned} M_{\text{FHSC}} &\approx k_L M_J^{\min} \left( \frac{T_{\text{ex}}}{T_{\text{ad}}} \right)^{\frac{3\gamma_1-4}{2\gamma_1-2}} \left( \frac{T_{\text{diss}}}{T_{\text{ex}}} \right)^{\frac{3\gamma_2-4}{2\gamma_2-2}} \\ &\approx 0.03 M_{\odot} \max \left( Z_d^{\frac{2}{4\beta+7}}, Z_d^{1/3} (u_{\text{rad}}/100 \text{ eV cm}^{-3})^{\frac{4\beta+1}{48}} \right) \end{aligned} \quad 6.$$

which is again quite insensitive to the opacity parameter  $Z_d$  except in radiation-dense, dust-rich environments.

Bound cores that do not grow to  $M_{\text{FHSC}}$  can still collapse, but over a Kelvin-Helmholtz timescale, an order-of-magnitude longer than the  $\sim 10^3 - 10^4\text{yr}$  accretion timescale generally required to reach  $M_{\text{FHSC}}$ . During this time a low-mass fragment can continue to accrete, or be accreted or disrupted by a more-massive core or protostar, so the formation of protostars with  $M \lesssim M_{\text{FHSC}}$  from normal fragmentation is likely rare. A low-mass truncation in the IMF at  $\sim M_{\text{FHSC}}$  is therefore expected, and indeed is found in numerical simulations. Recently Lee & Hennebelle (2018b) and Hennebelle et al. (2019) advocated for the importance of the FHSC in setting the peak of the IMF as described in Section 4.2.3.

### 3.2. Supersonic turbulence

Turbulence is ubiquitous in the ISM and comprehensive reviews have been dedicated to this topic (Mac Low & Klessen 2004; Elmegreen & Scalo 2004; McKee & Ostriker 2007; Hennebelle & Falgarone 2012). Here we focus the discussion on the aspects which are most fundamental in the context of star formation.

**3.2.1. Density PDF.** In a strongly compressible medium, such as isothermal gas, supersonic turbulence leads to a broad density distribution. This is because the fluid particles experience series of compressions induced by the ram pressure of the turbulent eddies. Several models have proposed that the turbulent density fluctuations constitute the seeds for the formation of future stars and may strongly influence the stellar mass spectrum (Padoan et al. 1997; Hennebelle & Chabrier 2008; Hopkins 2012b) as explained in Section 4.1.3.

Since the pioneering works of Vázquez-Semadeni (1994) and Nordlund & Padoan (1999) various simulations of hydrodynamic supersonic turbulence, have established that the density PDF is well represented by a log-normal form (e.g. Kritsuk et al. 2007; Federrath et al. 2008) given by

$$\mathcal{P}(\delta) = \frac{1}{\sqrt{2\pi\sigma_0^2}} \exp\left(-\frac{(\delta - \bar{\delta})^2}{2\sigma_0^2}\right), \quad \delta = \ln(\rho/\rho_0), \quad 7.$$

$$\bar{\delta} = -\sigma_0^2/2, \quad \sigma_0^2 \simeq \ln(1 + b^2 \mathcal{M}^2),$$

where  $\mathcal{M}$  is the Mach number,  $\rho_0$  is the mean density,  $\sigma_0$  is the variance of  $\delta$  and  $b \simeq 0.5 - 1$ . The origin of this log-normal PDF has been sought in the central limit theorem and the series of statistically independent shocks that swept the fluid particles. This picture has been recently further investigated by Rabatin & Collins (2022) which have calculated the density PDF that would result from a finite number of shocks leading to improve agreement with simulations.

Another useful formulation of the density PDF has been given by Hopkins (2013a) who has transposed the PDF obtained by Castaing (1996) to describe the velocity PDF of intermittent incompressible flows subject to a log-Poisson cascade. Confronting to large suite of numerical simulations, Hopkins (2013a) found that it provides excellent and robust fit.

**3.2.2. Scale dependence of flow quantities.** A very fundamental property of turbulence is that the flow quantities such as the mean velocity difference between two spatial locations at distance  $\delta l$  from each other, is scale dependent. Typically, it is generally assumed that in an homogeneous and isotropic flow (Kolmogorov 1941),

$$\frac{\rho \delta v^2}{\tau_{cross}} \simeq \frac{\rho \delta v^3}{\delta l} \simeq \epsilon, \quad 8.$$

where  $\tau_{cross} = \delta l / \delta v$  is the crossing time and  $\epsilon$  is the energy flux through scale. It is injected by some process, generally at large scales, and is usually dissipated at small scales through viscosity or other types of dissipation. This implies that between injection and dissipation, within the so-called inertial domain, one has  $\rho^{1/3} \delta v \propto \delta l^{1/3}$ . In incompressible fluids, this leads to the well known scaling relation  $E(k) \propto k^{-n+2}$ , where  $E(k)$  is the energy spectrum,  $k$  is the wavenumber and  $n = 2 + 5/3 = 11/3$ . Numerical simulations of supersonic isothermal flows have obtained similar values (Kritsuk et al. 2007; Federrath

2013). The velocity powerspectrum, which in incompressible flows, is identical to  $E(k)$ , has been found to be a little steeper and closer to  $n \simeq 1.9$ . Observationally, the velocity dispersion in molecular clouds has been observed to follow  $v_{rms} \simeq 1 \text{ km s}^{-1} (R/1 \text{ pc})^\eta$  where  $\eta = (n - 3)/2 \simeq 0.4 - 0.5$  (Larson 1981; Hennebelle & Falgarone 2012).

As for the density PDF, in various gravo-turbulent theories, the velocity scale dependence is playing a role in establishing the mass spectrum of the stellar progenitors either because of the turbulent support as inferred in Section 4.1.3 (Hennebelle & Chabrier 2008; Hopkins 2012b) or, see Section 4.1.6, through the distribution of converging flows (Padoan & Nordlund 2002).

### 3.3. Gravity, Jeans-instability and gravo-turbulence

Gravity in combination with the various *supports*, i.e. thermal, magnetic and turbulent is obviously the most important driver of star formation.

**3.3.1. Some fundamental aspects of gravity.** The most natural and well known timescale associated to gravity is the freefall time given by

$$\tau_{ff} = \sqrt{\frac{3\pi}{32} \frac{1}{G\rho}}, \quad 9.$$

which is used as a reference in many problems and essentially describes the time it takes for a cloud of density,  $\rho$ , and subject to its gravity only, to form a singularity.

In the absence of sufficient support, gravitational collapse occurs. Whereas the dynamics of pure self-gravitating gas is far beyond the scope of the present review, few results are worth mentioning. First, because the gravitational field derived from the gradient of a potential and because this potential is directly related to the density field through the Poisson equation, the gravitational force is stronger where the gradient of the density field is shorter. This implies that gravity tends to amplify anisotropies. Thus gravity tends to naturally form strongly anisotropic structures such as sheets and filaments (e.g. Lin et al. 1965; Smith et al. 2014). Second, as the collapse proceeds, density power-laws,  $r^{-\alpha}$ , develop. The most commonly reported exponents, at least in simulations and models, are  $\alpha = 2$  and  $\alpha = 3/2$ . They can be both understood in relatively simple terms. Since  $\rho v_r = \dot{M}/(4\pi r^2)$ , if the mass flux,  $\dot{M}$  is sufficiently stationary, a relation between  $\rho$  and  $v_r$  follows. Yet a good approximation for  $v_r$  is inferred from energy conservation leading to  $v_r \simeq \sqrt{2GM(r)/r}$ .

If the gas mass inside the sphere of radius,  $r$ , is dominated by a central object,  $M(r) \simeq M_*$ , we get  $v_r \propto r^{-1/2}$  and thus  $\alpha = 3/2$ . In the other case,  $M(r) \propto r^{3-\alpha}$ ,  $v_r \propto r^{1-\alpha/2}$  leading to the equation  $-\alpha + (1 - \alpha/2) = -2$  which admits  $\alpha = 2$  as a solution. These powerlaw density profiles have been inferred both from analytical self-similar solutions (Larson 1969; Penston 1969; Shu 1977) and from collapse calculations (Foster & Chevalier 1993).

A density profile  $\rho \propto r^{-\alpha}$  leads to a powerlaw density PDF. The number of fluid elements located between radius  $r$  and  $r + dr$  is given by  $dN \propto r^2 dr$  but since  $dr \propto \rho^{-1-1/\alpha} d\rho$ , we get

$$\mathcal{P}(\rho) = \frac{dN}{d \log \rho} = \rho^{-3/\alpha}. \quad 10.$$

For  $\alpha = 2$ , this leads to  $\mathcal{P}(\rho) \propto \rho^{-3/2}$ , while for  $\alpha = 3/2$ , we obtain  $\mathcal{P}(\rho) \propto \rho^{-2}$ . The

former behaviour is reported for high density gas in several simulations (e.g. Kritsuk et al. 2011).

The density PDF,  $\mathcal{P}(\rho) \propto \rho^{-3/2}$ , has been proposed to play an important role regarding the IMF as exposed in Section 4.1.4.

**3.3.2. Gravity and thermal support.** Thermal pressure is one of the support that can resist the gravitational force impeding gravitational collapse for spatial scales that are smaller than the so-called Jeans length

$$\lambda_{\text{Jeans}} = \sqrt{\pi} \frac{C_s}{\sqrt{G\rho}}, \quad 11.$$

where  $C_s$  is the sound speed. Equivalently if the mass contained inside a sphere of diameter  $\lambda_{\text{Jeans}}$  is smaller than the Jeans mass given by

$$M_{\text{Jeans}} = \frac{\pi^{5/2}}{6} \frac{C_s^3}{\sqrt{G^3\rho}} \approx 1.3M_{\odot} \left( \frac{n_{\text{H}}}{10^5 \text{ cm}^{-3}} \right)^{-1/2} \left( \frac{T}{10 \text{ K}} \right)^{3/2}. \quad 12.$$

thermal pressure can prevent gravitational collapse. This last expression reveals that a fundamental distinction has to be made depending on the effective adiabatic index,  $\Gamma_{\text{ad}}$ , where  $P \propto \rho^{\Gamma_{\text{ad}}}$ . Since  $C_s \propto \rho^{\Gamma_{\text{ad}}/2-1/2}$ , we see that if  $3\Gamma_{\text{ad}} - 4 > 0$ , the Jeans mass increases with density. This implies that if  $\Gamma_{\text{ad}} > 4/3$ , the gravitational collapse ends after some density enhancement because thermal support unavoidably dominates gravity if the gas contracts sufficiently, eventually leading to an equilibrium, e.g. in a hydrostatic stellar interior.

On the other hand, if  $\Gamma_{\text{ad}} < 4/3$ , the Jeans mass decreases with density showing that when collapse has started, thermal support becomes continuously weaker and the number of Jeans mass increases opening the possibility to the formation of several fragments. Obviously, it does not imply that equilibrium is not possible and various hydrostatic solutions are known. The simplest one, although due to instability never realised in realistic conditions, is probably the so-called singular isothermal sphere (SIS)

$$\rho(r) = \frac{C_s^2}{2\pi G r^2}. \quad 13.$$

As discussed in Section 3.3.1, an  $r^{-2}$  density profile also develops during collapse. Let us stress that the physical origin of these two  $r^{-2}$  profiles is entirely different.

Importantly  $\rho \propto r^{-2}$  implies that  $M(r) \propto r$ , meaning that most of the mass is found in the outer radii of a self-gravitating cloud. The general class of hydrostatic solutions have been described for instance in Bonnor (1956). The solutions have a finite density in the center unlike the SIS but approach a corresponding SIS solution at large radii. Therefore usually the solutions are simply cut at some radius, and it has been shown that only when the density contrast between the inner and outer density is below a certain threshold that the solution is stable. This lack of clear boundary definitions, constitutes a serious difficulty regarding the physical definition of dense cores (Section 2.3) in observations and in simulations.

The behaviour  $M(r) \propto r$  is a marked difference with the case  $\Gamma_{\text{ad}} > 4/3$  for which equilibrium solutions present a density that vanishes at some finite radius (in this respect the critical  $\Gamma_{\text{ad}}$  is  $\Gamma_{\text{ad}} = 6/5$ ). In practice, this means that whereas the definition of a self-gravitating structure with  $\Gamma_{\text{ad}} > 4/3$  is usually straightforward, this is not at all the

case for smaller  $\Gamma_{\text{ad}}$  and in particular for  $\Gamma_{\text{ad}} = 1$ . The influence of  $\Gamma_{\text{ad}}$  on the IMF is discussed in Section 5.2.1, 5.2.2 and 5.2.3.

**3.3.3. Gravity and turbulence.** Whereas they are often considered separately and even sometimes *opposed*, turbulence and gravity are tightly linked to each other leading to a concept sometimes named gravo-turbulence. It is for instance well established that turbulence is amplified and even generated during gravitational collapse (Robertson & Goldreich 2012; Guerrero-Gamboa & Vázquez-Semadeni 2020; Hennebelle 2021). On the other hand, turbulence plays a dual role with respect to the development of gravitational instability. Since as discussed in 3.2, stronger turbulence promotes the development of a higher fraction of dense gas, turbulence tends to trigger gravitational instability and induces fragmentation in smaller Jeans mass. However, in the same time turbulence may stabilize clouds that would otherwise be unstable. This effect is usually described as turbulent pressure (Bonazzola et al. 1987) and is a bit loosely described by replacing the sound speed by the velocity dispersion in Equation (12). Importantly, because the velocity dispersion increases with distance, the turbulent support unlike the sound speed, also tends to increase with scale. Whereas turbulent pressure is an elusive concept since turbulence decays in a crossing time, it must be understood in a dynamical sense. A cloud which is largely dominated by turbulence is typically dispersed in one turbulent crossing time and therefore does not collapse. Due to the dual roles played by turbulent, a broad mass spectrum is expected to be naturally produced by gravo-turbulence.

The density PDF in a self-gravitating and turbulent fluid can be viewed as a superposition of a low-density, turbulent part and a high-density, self-gravitating part (e.g. Kritsuk et al. 2011). This, in particular, implies that as expected, at high density the density PDF presents a powerlaw compatible with  $\simeq \rho^{-3/2}$ . This is because the very dense gas indeed forms under the influence of gravity. Interestingly, it has been found that the density fluctuations that develop on top of the mean density profile ( $\rho \propto r^{-2}$ ), appear to present a PDF that is close to a lognormal PDF with a width that would correspond to a PDF of an isothermal gas with  $\mathcal{M} \simeq 6$  turbulence (Hennebelle et al. 2019). The combination of high density gas associated to density turbulent fluctuations favors the formation of low mass objects during the collapse and may be at the origin of at least some of the brown dwarfs (e.g. Bonnell et al. 2008).

### 3.4. Ideal and non-ideal MHD

Magnetic field is ubiquitous in the ISM and magnetic energy is broadly comparable to kinetic and gravitational energies (Crutcher 2012) making magnetic field an important physical process to take into account although its exact importance remains controversial.

Magnetic field affects the gas dynamics in several ways and for a detailed discussions we refer to recent dedicated reviews (Hennebelle & Inutsuka 2019; Krumholz & Federrath 2019; Zhao et al. 2020).

The Lorentz force can be decomposed in two terms, namely the magnetic pressure and tension

$$\mathbf{F}_L = \frac{(\nabla \times \mathbf{B}) \times \mathbf{B}}{4\pi} = -\nabla \left( \frac{B^2}{8\pi} \right) + \frac{(\mathbf{B} \cdot \nabla) \mathbf{B}}{4\pi}, \quad 14.$$

Both terms play an important role regarding the support that magnetic field exerts against gravity. To quantify the importance of the magnetic support, let us consider a



spherical, uniform density cloud of mass  $M$  and radius  $R$ , threaded by a uniform magnetic field of intensity  $B$ . The magnetic flux that permeates the cloud is  $\Phi = \pi R^2 B$ . If the magnetic field is well coupled to the gas,  $\Phi$  is a conserved quantity. The ratio of magnetic over gravitational energies is thus

$$\frac{E_{\text{mag}}}{E_{\text{grav}}} = \frac{B^2 4\pi R^3 / 3}{8\pi} \times \frac{2R}{5GM^2} \propto \frac{B^2 R^4}{M^2} \propto \left(\frac{\Phi}{M}\right)^2. \quad 15.$$

Interestingly, the ratio of magnetic over gravitational energies does not depend on the cloud radius. This is for instance different for the thermal energy of an isothermal gas, which becomes smaller and smaller compared to the gravitational energy as the cloud collapses. From Equation (15), it appears that there is a critical value of the magnetic field strength for which the gravitational collapse is impeded when the cloud is compressed. If the mass-to-flux ratio is smaller than this critical value, it is said to be subcritical. It is called supercritical when the mass-to-flux is larger than the critical value. It is usual to define the parameter  $\mu = (M/\Phi)/(M/\Phi)_{\text{crit}}$ . A useful way to take into the influence of the magnetic field on the stability of a structure is to use the virial theorem which in the presence of magnetic field writes as

$$\langle V_{\text{rms}}^2 \rangle + 3 \langle C_s^2 \rangle + \frac{1}{2} \langle V_a^2 \rangle = -E_{\text{pot}}/M \quad 16.$$

where  $V_a = B/\sqrt{4\pi\rho}$  is the Alfvén speed. Note that in this expression, the surface terms to which we will not refer below have been dropped. An important relation which has been observed by several authors in numerical simulations, is that during collapse, the relation  $B \propto \sqrt{\rho}$  tends to hold (e.g. Lee & Hennebelle 2019; Guszejnov et al. 2020). This can likely be explained as follows (e.g. Basu 2000). Mass and flux conservation lead to  $B \propto \Sigma$  where  $\Sigma \propto \rho h$  is the column density and  $h$  is the altitude above the equatorial plane. Mechanical equilibrium along field lines leads to  $C_s^2 \propto \phi$  whereas with Poisson equation  $\phi/h^2 \simeq 4\pi G\rho$ . Combining these relations, we obtain  $B \simeq C_s/\sqrt{4\pi G\rho^{1/2}}$ . This implies that in Equation 16, the magnetic support behaves similarly to the sound speed. In particular, it is not expected to be scale dependent as it is the case for  $\langle V_{\text{rms}}^2 \rangle$ .

Due to the low ionisation in the dense ISM, the magnetic field is imperfectly coupled to the gas and non-ideal MHD corrections need to be taken into account. The typical time scale for ambipolar diffusion can be expressed as

$$\tau_{\text{ad}} \simeq \frac{4\pi\gamma_{\text{ad}}\rho\rho_i R^2}{B^2}, \quad 17.$$

where  $\gamma_{\text{ad}}$  is the ion-neutral friction coefficient and  $R$  is the spatial scale that is considered. Note that performing an accurate estimate of the ionisation and of the charge carriers is necessary to get accurate resistivities (e.g. Zhao et al. 2020), particularly at high densities. In order to estimate  $\tau_{\text{ad}}$ , one usually considers that the cloud is in virial equilibrium,  $B^2/4\pi \simeq M\rho G/R$  (within a factor of a few). (Shu et al. 1987) found that for densities on the order of  $10^5 \text{ cm}^{-3}$ ,  $\tau_{\text{ad}}/\tau_{\text{ff}} \simeq 8$ . This high value may explain why observed cores do not appear to be far from being critical. Much lower values of  $\tau_{\text{ad}}/\tau_{\text{ff}}$  may arise at larger densities (e.g. Zhao et al. 2020) and this may have a critical impact regarding fragmentation and disk formation.

Another fundamental aspect of magnetic field, particularly relevant in the context of collapsing cloud is the so-called magnetic braking. Magnetic tension allows the propagation



of torsional Alfvén waves, which transfer angular momentum through the cloud (Shu et al. 1987; Zhao et al. 2020). To estimate the typical time scale for magnetic braking, let us consider an intercloud medium of density  $\rho_{\text{icm}}$  and a magnetic field parallel to the rotation axis. The waves propagate at the Alfvén speed,  $V_a = B/\sqrt{4\pi\rho_{\text{icm}}}$  along a cylinder parallel to the magnetic field. Magnetic braking is significant when the waves have transmitted to the intercloud medium a substantial fraction of the cloud angular momentum and this occurs when the Alfvén waves have propagated at a distance from the cloud,  $l$ , such that  $l \times \rho_{\text{icm}} \simeq R \times \rho_0$ . An estimate for the magnetic braking time, in case where the magnetic field and the rotation axis are aligned is thus:

$$\tau_{\text{br}} \simeq \frac{R}{V_a} \frac{\rho_0}{\rho_{\text{icm}}}. \quad 18.$$

The braking time increases when  $\rho_{\text{icm}}$  decreases because if the density of the intercloud medium is low, its inertia is also low and the transfer of angular momentum is rather inefficient. The impact that the magnetic field may have on planet-forming disks is expected to be very significant (Zhao et al. 2020) as recently confirmed by numerical simulations where disk populations are inferred (Lebreuilly et al. 2021).

### 3.5. Tidal forces and tidal radius

**3.5.1. Tidal forces.** Generally speaking, gravitational forces vary in space and this implies that finite size objects that sit in external gravitational potential,  $\phi$ , experience gradients of external gravitational force. These gradients are known as tidal forces and tend to modify the shape and the evolution of the objects. When the size of the object remains small compared to the characteristic scale of the external gravitational potential, it is meaningful to expand the gravitational force around the center of mass leading to a tidal tensor (e.g. Colman & Teyssier 2020)

$$g_i = T_{ij}x_j, \quad T_{ij} = \frac{\partial^2 \phi}{\partial x_i \partial x_j}. \quad 19.$$

Since this tensor is symmetrical it can be diagonalised, which restricts the problem to three eigenvalues,  $\lambda_1$ ,  $\lambda_2$  and  $\lambda_3$ . Poisson equation leads to  $\lambda_1 + \lambda_2 + \lambda_3 = -4\pi G\rho$ . In spherical geometry,  $\lambda_1 = \partial^2 \phi / \partial r^2$ , while  $\lambda_2 = \lambda_3 = r^{-1} \partial \phi / \partial r$ . Thus for a density profile  $\rho = \rho_0 (r/r_0)^{-\alpha}$ , this leads to  $\lambda_1 = 4\pi G\rho(1-\alpha)/(3-\alpha)$  and  $\lambda_2 = \lambda_3 = 4\pi G\rho/(3-\alpha)$ . Thus we see that if  $\alpha < 1$  (resp  $\alpha > 1$ ), the radial component of the tidal tensor,  $\lambda_1$ , is negative (positive), implying that the tidal forces tend to compress (shear) the piece of fluid. In particular, this implies that a piece of gas that sits within a significant external potential, can be either more or less prone to collapse.

**3.5.2. Tidal radius.** Given two stars of masses  $m$  and  $M$  and located at a distance  $D$ , the question arises on which of these two stars a fluid element will eventually be accreted. The classical estimate (e.g. Binney & Tremaine 2008) considers that the critical radius, also named tidal radius, is given by the location where the gravitational force vanishes. Assuming that  $m \ll M$ , one can show that this radius, also named the Jacobi radius and used as a proxy for the tidal radius is given by

$$R_{\text{tidal}} \simeq R_J = \left( \frac{m}{3M} \right)^{1/3} D. \quad 20.$$

In the context of the IMF, tidal forces have been advocated to play an important, although quite different, role respectively by [Bonnell et al. \(2001\)](#) and by [Lee & Hennebelle \(2018b\)](#) and [Colman & Teyssier \(2020\)](#). The former propose that the tidal radius may contribute to establish the powerlaw behaviour of the IMF by regulating the accretion rate in cluters (Section 4.1.1) whereas the latter argue that tidal forces contribute to set the characteristic mass of stars, i.e. the mass at which the IMF peak occurs, by preventing fragmentation in the neighborhood of an existing first hydrostatic core or young stellar object (see Section 4.2.3).

### 3.6. Accretion

The specific rate of accretion can be important for the IMF in several ways. The accretion timescale  $t_{\text{acc}} = M/\dot{M}$  is one the key timescales for protostellar evolution (see Section 3.7), which for instance determines the rate of accretion-powered feedback such as outflows and radiation.  $t_{\text{acc}}$  also determines the time available to gather mass before disruptive processes can intervene and terminate accretion, e.g. dynamical interactions or disruption of the host cloud by feedback.

The mass accreted by a star can be roughly divided into two parts. Initially, the gravity in a protostellar core is dominated by gas self-gravity, and gas will accrete onto the protostar at a rate that is essentially independent of the mass of the star. [Shu \(1977\)](#) derived a spherically-symmetric, self-similar solution for collapse of a  $\propto r^{-2}$  density profile from rest:

$$\dot{M} = 0.975 f(A) \frac{C_s^3}{G}, \quad 21.$$

where  $f(A) \geq 1$  depends on the instability parameter  $A = 4\pi r^2 \rho(r) G / C_s^2$ , with  $A = 2$  being the threshold of collapse, and  $f(A) \propto A$  for  $A \gg 2$ . For instance the self-similar collapse solution inferred by [Larson \(1969\)](#) has  $A = 8.86$  while in collapse calculations (e.g. [Foster & Chevalier 1993](#); [Gong & Ostriker 2015](#)), the value of  $A$  which varies with time, is several times higher than 2 at the early stage and eventually drops below this value. Note the lack of explicit dependence of  $\dot{M}$  on the current stellar mass  $M_*$  – there is always central region of supersonic flow where stellar gravity dominates and  $v \approx \sqrt{GM_*/r}$ , but the rate-limiting step for accretion is the initial infall determined by gas dynamics and microphysics. Also note that  $\dot{M}$  is simply  $\propto M(< r) / t_{\text{ff}}(< r)$  evaluated from the enclosed mass and mean density within any radius  $r$ . This collapse on the gas free-fall timescale is a distinguishing feature of “core accretion” scenarios in general, including turbulent cores forming massive stars (e.g. [McKee & Tan 2003](#)).

In the opposite regime, the gravity of the star itself is the causal factor that diverts gas into the accretion flow. In this case the accretion rate may be written

$$\dot{M} = \pi \rho V_{\text{rel}} R_{\text{acc}}^2, \quad 22.$$

where  $R_{\text{acc}}$  is the critical impact parameter for gravitational capture of a gas element. The canonical example is Bondi-Hoyle-Lyttleton (BHL) accretion (e.g. [Edgar 2004](#)), where a point mass captures gas while moving at a speed  $v_\infty$  relative to a uniform gas medium with density  $\rho_\infty$  and sound speed  $c_\infty$ . In an isothermal medium, the rate of BHL accretion may

be approximated by (e.g. [Ruffert 1996](#)):

$$\dot{M}_{\text{BHL}} \approx 4\pi\rho_\infty G^2 M^2 c_\infty^{-3} \left[ \frac{\lambda^2 + \mathcal{M}^2}{(1 + \mathcal{M}^2)^4} \right]^{1/2} \quad 23.$$

where  $\mathcal{M} = v_\infty/c_\infty$  and  $\lambda \sim 1.1$  is measured from hydrodynamics simulations.

Naturally the behaviour is more complex in real turbulent, inhomogeneous, magnetized, giant molecular clouds. The time dependence of the ambient flow makes the accretion stochastic, but scale-free simulations still find the mean accretion rate is proportional to the BHL rate ([Krumholz et al. 2006](#)). Magnetic fields can also support gas against infall, and this effect can be modeled by the usual substitution  $\mathcal{M}^2 \rightarrow \mathcal{M}^2 + k\mathcal{M}_A^2$  in Equation 23 ([Lee et al. 2014](#)).

In turbulent, self-gravitating flows, the effective values of  $v_\infty$  and  $\rho_\infty$  must also be considered scale-dependent, and  $v_\infty$  can be much smaller if there is correlation between the stellar and gas kinematics. Therefore  $\dot{M}_{\text{BHL}}$  can be much larger than the fiducial value estimated in Equation 23, and simple hydrodynamics experiments have found that this mode of accretion can contribute appreciably to the growth of massive stars in dense star clusters ([Bonnell et al. 2001, 2006](#); [Ballesteros-Paredes et al. 2015](#); [Kuznetsova et al. 2017](#)) possibly shaping the high-mass IMF (see Section 4.1.1). It has not yet been shown explicitly that accretion proceeds in this way once other important processes such as feedback and self-consistent MHD turbulence are accounted for, and [Tan et al. \(2014\)](#) estimated that even a conservative amount of outflow feedback momentum could present a severe obstacle to accretion of gas beyond the natal dense, turbulent core. On the other hand, ([Smith et al. 2009](#)) and [Gong & Ostriker \(2015\)](#) do not find bound gas cores massive enough to form massive stars, requiring a more extended accretion scenario. Similarly, the multi-physics simulation in [Grudić et al. \(2022\)](#) found massive stellar accretion timescales too long to be accounted for by accretion from dense cores alone.

### 3.7. Stellar evolution and feedback

Once collapse to protostellar densities has occurred, the protostar’s evolution may affect the IMF because the stellar properties determines the star’s various rates of mass, momentum, and energy feedback. The stellar mass-radius relation determines the strength of accretion-powered processes such as protostellar jets and outflows and radiation. And once on the main sequence, a star’s evolution and energetics of radiation and stellar winds are largely determined by its main-sequence mass. Here we will focus on the aspects of stellar evolution that are most relevant for determining feedback rates.

Once the dissociation of  $\text{H}_2$  is complete, quasi-isothermal collapse can no longer proceed, and the protostar will again assume a hydrostatic, approximately-polytropic structure with a certain outer radius  $R_\star$  and a central temperature

$$T_c \approx 0.5\beta_c \frac{\mu m_p}{k_B} \frac{GM}{R} \quad 24.$$

where  $\mu \sim 0.613$  is the mean molecular weight for ionized stellar interiors and  $\beta_c$  is ratio of gas to total pressure in the center (the latter expression assumes  $\beta_c \sim 1$ , valid except for  $\gtrsim 10M_\odot$  stars). Once nuclear burning has begun,  $T_c$  will be vary only weakly due to the steep dependence of the reaction rate on temperature, first at  $\sim 1$  MK for D burning and then  $\gtrsim 15$  MK for the various H burning processes. A hydrostatic protostar’s internal

dynamical time is much shorter than any other relevant timescale, and evolution will take place over the timescales required for the star’s mass and energy to change, e.g. the accretion time

$$t_{\text{acc}} = \frac{M}{\dot{M}} = 10^5 \text{ yr} \left( \frac{M}{M_{\odot}} \right) \left( \frac{\dot{M}}{10^{-5} M_{\odot} \text{ yr}^{-1}} \right), \quad 25.$$

and the Kelvin-Helmholtz time

$$t_{\text{KH}} = \frac{GM^2}{R_{\star} L_{\star}} = 3 \times 10^5 \left( \frac{M}{M_{\odot}} \right)^2 \left( \frac{R_{\star}}{R_{\odot}} \right)^{-1} \left( \frac{L_{\star}}{10 L_{\odot}} \right)^{-1} \text{ yr}, \quad 26.$$

where  $L_{\star}$  is the the rate of energy transfer from the interior of the protostar. At early times, when  $t_{\text{acc}} \ll t_{\text{KH}}$ , emission from the star is dominated by the accretion luminosity:

$$L_{\text{acc}} = f_{\text{acc}} \frac{GM\dot{M}}{R_{\star}} = 30 L_{\odot} f_{\text{acc}} \left( \frac{\dot{M}}{10^{-6} M_{\odot} \text{ yr}^{-1}} \right) \left( \frac{M}{M_{\odot}} \right) \left( \frac{R_{\star}}{R_{\odot}} \right)^{-1} \quad 27.$$

and the protostar grows in mass and radius with an energy and entropy budget determined by the energetics of the gas as it reaches  $R_{\star}$ . Eventually, when  $t_{\text{KH}} \lesssim t_{\text{acc}}$ , or equivalently  $L_{\star} \gtrsim L_{\text{acc}}$ , the star contracts with a luminosity  $L_{\star} \sim 4\pi R_{\star}^2 \sigma_{\text{SB}} T_{\text{eff}}^4$ . The overall sequence is one of initial growth in radius followed by contraction to the star’s eventual main-sequence radius (Palla & Stahler 1991; Nakano et al. 2000; Hosokawa & Omukai 2009). This evolution in radius must be accounted for to model the effects of accretion-powered feedback.

**3.7.1. Protostellar outflows.** Only a certain fraction of the gas captured by a protostar will end up accreting onto the protostar itself: the remainder should be ejected in a magnetocentrally-powered outflow (Blandford & Payne 1982; Shu et al. 1988; Pelletier & Pudritz 1992). This naturally explains the ubiquity of bipolar protostellar outflows in star-forming, as evidenced by optical Herbig-Haro objects at the shocked interface with the ambient medium, cavities imaged in cold molecular emission, and warm molecular emission from the jet. For a review of observations of protostellar outflows see (Bally 2016). Very recently, JWST has imaged the warm molecular component from protostellar jets with order-of-magnitude finer resolution than Spitzer (Ray et al. 2023).

Some details of the jet launching mechanism remain uncertain: MHD disk wind models have been studied extensively, but typically under the assumptions of axisymmetry and steady inflow, which is unlikely to fully describe the conditions in accreting protostellar envelopes. The magnetic field structure and the degree of misalignment between the disk and the large-scale magnetic field, can both affect the strength and collimation pattern of the outflows (Gerrard et al. 2019).

Current 3D models cannot simultaneously resolve the jet launching zone near the star and the larger cloud environment and star cluster, so IMF calculations have adopted sub-grid prescriptions describing the velocity, mass load, and collimation pattern of the jets. For a magnetocentrifugal wind, the natural parametrization for the jet speed is

$$v_w = f_K \sqrt{\frac{GM}{R_{\star}}}, \quad 28.$$

and one may assume a certain fraction  $f_w$  of the mass that accretes near the protostar is launched in the wind. These parameters  $f_w$  and  $f_K$  are somewhat constrained by observations: it is possible to measure the momentum present in protostellar outflows, and to compare with the corresponding luminosity of the young stellar object launching the jet

(e.g. [Maud et al. 2015](#)). Typical parameters adopted by star cluster formation simulations are  $f_w \sim 0.1 - 0.3$  and  $f_K \sim 0.3 - 1$  ([Cunningham et al. 2011](#); [Federrath et al. 2014](#)), and a collimated angular pattern of mass and momentum deposition is typically assumed (e.g. [Matzner & McKee 1999](#)). The addition of protostellar outflows to numerical models tends to have a dramatic effect on the predicted stellar mass spectrum, due to their effects on the transport of both gas and radiation (§5.7).

**3.7.2. Stellar winds.** Winds from intermediate- and high-mass stars can contribute appreciably to the stellar feedback from a young star cluster, potentially affecting the growth of individual stars (e.g. [Rosen et al. 2021](#); [Rosen 2022](#)) or the unbinding of gas from the cluster’s natal clump ([Dale et al. 2013](#); [Rogers & Pittard 2013](#)), both of which may affect the IMF. Metal ion transitions contribute most of the radiative force driving O star winds, so these are expected to be metallicity-dependent, generally scaling roughly as  $\dot{M} \propto Z^{0.7} - Z^{0.9}$  ([Vink et al. 2001](#)). The onset of the Wolf-Rayet phase increases the mass-loss rate by about an order of magnitude. The terminal velocity of the wind is generally proportional to the stellar escape speed, with  $v_{\text{wind}} = A\sqrt{2GM/R_*}$ ,  $A \sim 1.3$  for  $T_{\text{eff}} < 21\text{ kK}$  and  $A \sim 2.6$  for  $T_{\text{eff}} > 21\text{ kK}$  ([Lamers et al. 1995](#)). A recent set of evolutionary tracks and mass-loss histories for single massive stars of varying metallicity is presented in [Szécsi et al. \(2022\)](#).

**3.7.3. Stellar radiation.** Radiation from stars and protostars can influence the IMF in numerous ways, affecting both the thermal structure and the dynamics of the star-forming gas flow. In the absence of massive stars, the radiation field is dominated by accretion-powered radiation (Equation 27), with a typical light-to-mass ratio of order  $10 - 100L_{\odot} M_{\odot}^{-1}$ . Once massive ( $\gtrsim 8M_{\odot}$ ) stars form, they quickly reach the main sequence and start moving along it as they accrete, and their fusion-powered radiation comes to dominate radiation field in the protocluster ([Grudić et al. 2022](#)). A fit to the zero-age main sequence luminosity of the [Szécsi et al. \(2022\)](#)  $9 - 500M_{\odot}$  stellar models gives

$$L_{\text{MS}} = 4.5 \times 10^5 L_{\odot} \left( \left( \frac{M}{20M_{\odot}} \right)^{-1.3} + \left( \frac{M}{20M_{\odot}} \right)^{-0.33} \right)^{-3.3}, \quad 29.$$

with no strong dependence on metallicity. Radiation from a massive star emerges primarily as UV, but if the star is accreting then the photons will be absorbed by dust and neutral gas, and the emergent radiation will be primarily at  $\sim 10\mu\text{m} - 1\text{mm}$  wavelengths. In the IR-dominated regime, the structure of the radiation field is determined by the gas/dust density profile and radius of the photosphere ([Chakrabarti & McKee 2008](#)).

Whatever the source of the radiation, (proto-) stellar emission will nearly always dominate over the initial ambient radiation field near the protostars, determining the dust temperature and hence the thermal structure and Jeans mass dense gas in protostellar disks and envelopes, which can be an important regulator of the IMF ([Offner et al. 2009](#); [Krumholz 2011](#); [Guszejnov et al. 2016](#); [Hennebelle et al. 2022](#)). Radiation pressure of optically-thick infrared radiation on dust in optically-thick accreting envelopes can also influence the upper end of the IMF by moderating massive stellar accretion ([Larson & Starrfield 1971](#)), although it cannot stop it entirely if the gas flows in a disk or filamentary geometry ([Krumholz et al. 2009](#); [Kuiper et al. 2010](#)). This IR radiation effect pressure depends on dust abundance and opacity, and hence metallicity.

Lastly, radiation plays an important role in cutting off the overall gas supply for star formation, unbinding gas from the cloud through some combination of cloud-scale radiation pressure on dust grains and gas pressure-driven HII region expansion, depending on the density and dust abundance/opacity of the cloud (Krumholz & Matzner 2009; Kim et al. 2016). Once the cloud is dispersed, both fragmentation and accretion cease and the stellar mass spectrum is set.

**3.7.4. Supernovae.** Most stars more massive than  $\sim 8M_{\odot}$  will end their lives in an energetic ( $\sim 10^{51}$ erg) core-collapse supernova, ejecting most of their mass and leaving behind a remnant. This form of feedback regulates galactic star formation and enriches the ISM, setting the mass and chemical composition of galaxies (Naab & Ostriker 2017). SNe regulate the level of turbulence in a galaxy, and hence cloud properties and the initial conditions for star formation (Lu et al. 2020; Ostriker & Kim 2022). But the IMF in a given star cluster is not likely affected by SNe *from that cluster*, because the soonest they can happen is after the  $\sim 3$  Myr lifetime of a very massive star. This can be further delayed depending on the specifics of which stellar masses explode and binary mass transfer (Heger et al. 2023), and the additional assembly time required for massive stellar accretion (Grudić et al. 2022). Protostellar outflows, radiation, and stellar winds are all active during this time, so cloud-scale experiments starting from a starless state find that supernovae tend to come too late to strongly influence the dynamics of star formation on GMC or star cluster scales (Grudić et al. 2019), or are even relatively ineffective in molecular cloud environments (Walch & Naab 2015; Geen et al. 2016). In observations,  $\lesssim 3$  Myr old, exposed star clusters are common, implying that early feedback alone is sufficient to end the embedded phase of a cluster in many cases (Hollyhead et al. 2015).

## 4. Overview of IMF theories - Success and limit

Numerous analytical theories have been developed through years to explain the physical origin of the IMF. They broadly fall in two categories, the theories that have attempted to explain the peak of the IMF, that is to say explain the origin of a characteristic mass, and the theories that tried to explain the mass spectrum of higher mass stars.

### 4.1. How to explain a broad mass spectrum of stars?

The exact shape of the IMF for  $M > 1 M_{\odot}$  is still discussed. It is possibly a power-law, a lognormal or a combination of the two. At first sight it does not seem to present a characteristic scale or mass and is more accurately described as a scale-free process something that for instance turbulence and also gravity tend to produce. The challenge is therefore to understand how exactly this may work and which process, if any, is dominant. The first models which have been proposed (Hoyle 1953; Larson 1973; Elmegreen & Mathieu 1983; Zinnecker 1984) were based on the general idea that star forming clouds would recursively fragment with equal and independent probability at each step.

Nowadays, the proposed explanations fall, broadly speaking, in two categories whose main differences rely on the importance of an initial *deterministic* mass accretion reservoir. Theories based on nearly stochastic accretion (Basu & Jones 2004; Maschberger et al. 2014), for instance competitive accretion (Bonnell et al. 2001), assume that most of the mass accreted by a star, is not provided by a preexisting gas reservoir but largely the result

of nearly random processes. On the other-hand, gravo-turbulent theories (Inutsuka 2001; Padoan & Nordlund 2002; Hennebelle & Chabrier 2008; Hopkins 2012b) emphasize the role of a coherent mass of gas, a reservoir, that is typically set by turbulence and *already exists* when the protostar first forms.

While these scenarios have often been presented as being exclusive from each other, it is likely the case that they both contribute to the final stellar mass spectrum.

**4.1.1. Competitive accretion.** Competitive accretion is probably the first model, based on stochastic accretion to have been developed. It has been proposed by Zinnecker (1982) and then further elaborated by Bonnell et al. (2001) (see also Hsu et al. 2010; Maschberger et al. 2014; Ballesteros-Paredes et al. 2015; Kuznetsova et al. 2017, 2018). In this scenario, the gas accretion onto a star increases with its mass, because of the stronger gravitational influence, it has on the surrounding medium. Thus the more massive stars attract more gas than the less massive ones, and therefore tend to become even more massive.

The accretion rate is given by Equation 22, and to estimate the different factors and make specific predictions, Bonnell et al. (2001) have considered two cases, namely where the gravitational potential is dominated by the gas or by the stars as expected in an older cluster.

**Gas dominated potential.** Bonnell et al. (2001) considered that the gas density is proportional to  $r^{-2}$ , where  $r$  is the radial coordinate. They further assume that the stellar density,  $n_*$ , also follows  $n_* \propto r^{-2}$ . The accretion radius,  $R_{acc}$  is assumed to be equal to the tidal radius given by Equation 20 with  $m = M_*$  and  $M = M_{enc}$  where  $M_{enc}$  is the cluster mass enclosed within radius  $r$  and  $M_*$  is the mass of an individual star. Since the mass of gas  $M(r) \propto r$ , the infall speed is about  $V_{in} \simeq \sqrt{GM(r)/r}$ . Assuming that the stars have virialized velocities leads to  $V_{rel} \simeq V_{in}$ . The number of stars,  $dN_*$ , located between  $r$  and  $r + dr$  is  $dN_* = n_*(r) \times 4\pi r^2 dr \propto dr$ . Thus Equation 22 leads to  $\dot{M}_* \propto (M_*/r)^{2/3}$ . Therefore, after integration, assuming that stars remain at the same distance,  $r$ , during the accretion process, we obtain  $M_* \propto r^{-2}$ ,  $r \propto M_*^{-1/2}$  and consequently:

$$dN_* \propto M_*^{-3/2} dM_*, \quad 30.$$

implying  $\Gamma_{IMF} = -1/2$ .

**Star dominated potential.** Assuming the potential is dominated by stars located in the cloud center, the density would then be given by  $\rho \propto r^{-3/2}$  (see Section 3.3.1),

The accretion radius is now supposed to correspond to the Bondi-Hoyle radius since the star and gas velocities are not correlated anymore. This leads to  $\dot{M}_* = \pi \rho V_{rel} R_{BH}^2$  where  $R_{BH} \propto M_*/V_{rel}^2$  (see Section 3.6), and it follows that

$$\dot{M}_* \propto M_*^2. \quad 31.$$

Bonnell et al. (2001) show that under reasonable assumptions this would lead to  $dN \propto M_*^{-2} dM_*$  or equivalently  $dN/d \log M \propto M^{-1}$  implying  $\Gamma_{IMF} = -1$ .

These stellar distributions seem to be confirmed by the simulations presented in Bonnell et al. (2001) and Hsu et al. (2010) which consist in placing randomly sink particles in a molecular cloud and letting them accrete. In these experiments a power-law with  $\Gamma_{IMF} \simeq$



-1 develops. The predicted exponents,  $\Gamma_{IMF} = -0.5$  and -1 are close, although slightly shallower than, the Salpeter exponent,  $\Gamma_{IMF} \simeq -1.3$ .

**4.1.2. Stochastic accretion.** Several studies (Basu & Jones 2004; Myers 2009; Dib et al. 2010; Maschberger 2013b; Basu et al. 2015) have investigated the scenario in which the gas accretion onto the star is proportional to some powerlaw of the mass of the stars and is then stopped by a stochastic process which can be either the finite reservoir of mass, an outflow or an HII region that would sweep up the remaining gas within the vicinity of the accreting protostar or an N-body gravitational interaction that would eject the stars from the gas rich region.

The first models were proposed by Silk (1995) and Adams & Fatuzzo (1996). They start by relating the mass of the stars to the physical parameters of the cloud such as sound speed and rotation and then assume that an outflow whose properties are related to the accretion luminosity stops the cloud collapse. Using the Larson relations (Larson 1981), all these parameters are linked to the clump masses. Using the mass spectrum of the clumps (e.g. Hennebelle & Falgarone 2012), they inferred the IMF.

Basu & Jones (2004) have developed a quantitative statistical approach. It is assumed that initially, due to the large number of processes that control their formation (and invoking the central limit theorem) the dense core distribution is simply lognormal. The cores are then assumed to grow by accretion with an accretion rate that is proportional to their mass,  $\dot{M} = \gamma M \rightarrow M(t) = M_0 \exp(\gamma t)$ , leading to  $\log M = \mu = \mu_0 + \gamma t$ . Finally, accretion is assumed to last over a finite period of time given by  $f(t) = \delta \exp(-\delta t)$ . The star mass distribution is thus obtained by summing over the accretion time distribution.

$$f(M) = \int_0^\infty \frac{\delta \exp(-\delta t)}{\sqrt{2\pi}\sigma_0 M} \exp\left(-\frac{(\ln M - \mu_0 - \gamma t)^2}{2\sigma_0^2}\right) dt \quad 32.$$

$$= \frac{\alpha}{2} \exp(\alpha\mu_0 + \alpha^2\sigma_0^2/2) M^{-1-\alpha} \operatorname{erf}\left(\frac{1}{\sqrt{2}}\left(\alpha\sigma_0 - \frac{\ln M - \mu_0}{\sigma_0}\right)\right),$$

where  $\alpha = \delta/\gamma$  and  $\sigma_0$  determine the width of the initial dense core distribution. Since  $\delta$  and  $\alpha$  derived from the same physical processes, their ratio is assumed to be close to unity and thus  $f(M)$  is expected to present a powerlaw behaviour close to the observed IMF.

Bate & Bonnell (2005) have presented another related model based on an idea proposed by Price & Podsiadlowski (1995). Some of the objects that form by fragmentation within clusters are being ejected through N-body gravitational interaction with the other objects. Once ejected, the objects stop accreting further gas. Assuming a lognormal accretion rate and an exponential probability of being ejected, a mass distribution is obtained and it is shown that it can fit the IMF for some reasonable choices of parameters. Myers (2009) developed a model that rely on similar ideas considering the accretion coming from the surrounding background. Adjusting two parameters, the observed IMF is well reproduced (his figure 5).

**4.1.3. Gravo-turbulent theory in a turbulent density field.** Whereas in the accretion models, turbulence is not determinant, it is one of the essential physical processes for the gravo-turbulent theories presented below, although the role it plays differs between models.

The first theory which combined turbulence and gravity was proposed by Padoan et al. (1997). The authors consider a lognormal density distribution (see Section 3.2.1) and select the regions of the flow which are Jeans unstable. By doing so, they get too steep an IMF



(typically  $dN/dM \propto M^{-3}$ ) but nevertheless find a lognormal behaviour at small masses, a direct consequence of the lognormal density distribution, and a powerlaw one at large masses.

[Hennebelle & Chabrier \(2008\)](#) (see also [Chabrier et al. 2014](#)) proposed an approach which consists in counting the mass of the gas for which gravity supersedes all supports, namely thermal, turbulent and magnetic, according to the virial theorem. In this theory, turbulence possesses a dual role. On one hand it enhances star formation by locally compressing the gas within shocks and this is accounted for in the density PDF. On the other hand, it also exerts a support to gravity through turbulent dispersion.

The theory is an extension of the [Press & Schechter \(1974\)](#) statistical formalism, developed in cosmology. Two significant differences are *i*) the density field, which in cosmology is characterized by small and Gaussian fluctuations and by a lognormal PDF with very large fluctuations in molecular clouds, and *ii*) the selection criterion, which is a simple scale-free density threshold in cosmology and scale-dependent, based on the virial theorem in the star formation case.

More precisely, fluid particles which are dominated by their internal gravity as specified by Equation 16 are assumed to undergo gravitational collapse and form stars. This leads to the definition of a critical mass,  $M_R^c$  and of a critical density,  $\rho_R^c$ , which generally depend on the spatial scale  $R$ .

The method entails the following steps. First, using a prescribed window function, the density field is smoothed at a scale  $R$ . Then, the total mass contained in sphere which, at scale  $R$ , present a density larger than the critical density,  $\rho_R^c$ , is obtained by integrating the density PDF from  $\rho_R^c$  to infinity. This mass, on the other hand, is also equal to the total mass of the stars having a mass lower than  $M_R^c$ . This leads to

$$\int_{\delta_R^c}^{\infty} \bar{\rho} \exp(\delta) \mathcal{P}_R(\delta) d\delta = \int_0^{M_R^c} M' \mathcal{N}(M') P(R, M') dM'. \quad 33.$$

In this expression,  $M_R^c$  is the mass which at scale  $R$  is gravitationally unstable,  $\delta_R^c = \log(\rho_R^c/\bar{\rho})$  and  $\rho_R^c = M_R^c/(C_m R^3)$ ,  $C_m$  being a dimensionless coefficient of order unity.  $\mathcal{P}_R$  is the density PDF, while  $P(R, M')$  is the conditional probability to find a gravitationally unstable mass,  $M'$  embedded into  $M_R^c$  at scale  $R$ , which is usually assumed to be equal to 1.  $\mathcal{N}$  is the mass spectrum of the stars that eventually form.

The derivative of Equation (33) with respect to the spatial scale  $R$ , leads to the mass spectrum

$$\mathcal{N}(M_R^c) = \frac{\bar{\rho}}{M_R^c} \frac{dR}{dM_R^c} \left( -\frac{d\delta_R^c}{dR} \exp(\delta_R^c) \mathcal{P}_R(\delta_R^c) + \int_{\delta_R^c}^{\infty} \exp(\delta) \frac{d\mathcal{P}_R}{dR} d\delta \right). \quad 34.$$

While the second term is important to explain the mass spectrum of unbound clumps defined by a uniform density threshold, in most cases, it plays a minor role for gravitationally bound mass reservoir and can generally be dropped.

Using the lognormal density PDF as specified by Equation 7, and using the expression of  $\rho_R^c$  and  $M_R^c$ , one obtains an expression for the mass spectrum. When the turbulent support is negligible with respect to the thermal one, with Equation (34) it can be shown that at large masses the mass spectrum is identical to the [Padoan et al. \(1997\)](#) result, i.e.  $dN/d\log M \propto M^{-2}$ ,  $\Gamma_{IMF} = -2$ . However, when the turbulent support is significant,

$$\frac{dN}{d\log M} \propto M^{-(n+1)/(2n-4)}, \quad 35.$$

where the index of the velocity powerspectrum  $n$  is related to  $\eta$  by the relation  $\eta = (n-3)/2$  and where we remind that  $v_{rms} \propto R^\eta$ . As  $n \simeq 3.8-3.9$  in supersonic turbulence simulations (see Section 3.2.2), turbulent dispersion leads to an exponent that is very close to the Salpeter  $\Gamma_{IMF} = -1.3$  value.

Detailed comparisons with numerical simulations of supersonic isothermal turbulence were carried out in Schmidt et al. (2010). The mass spectrum of *cores* supported either by pure thermal support or by turbulent plus thermal support has been computed and show very good agreement with the present theory, suggesting that indeed, turbulent support is needed to yield the Salpeter index. Note that Schmidt et al. (2010) use for the density PDF the one they measure in their simulations which is nearly, but not exactly lognormal. Most importantly one should stress that indeed the theory presented by Hennebelle & Chabrier (2008) as well as these simulations were not truly self-gravitating as they do not entail collapse density PDF (Equation 10). This is a major restriction, particularly for low mass stars, as discussed in Section 4.1.4.

A complementary formulation has been proposed by Hopkins (2012a,b, 2013b) using excursion set theory (Zentner 2007). This approach consists in performing random walks in the Fourier space of the density field. Essentially a random point in the field is picked and the gas density around that point is computed using a window of some specified radius. As this radius increases from zero to some maximum value, the mean density in the window can be compared to the, scale dependent, critical density, also named the barrier, obtained from virial theorem as specified in Equation 16 and as explained above contained the various supports. Note that Hopkins (2012a) propose a global model that includes spatial scales larger than that of molecular clouds to describe the whole galactic disc. An appealing concept is that the clouds are defined as density fluctuations that first cross the collapse threshold. More precisely when the spatial scale is decreased, the first crossing is the first time that self-gravity becomes dominant. These density fluctuations present a mass spectrum that is slightly shallower than  $\Gamma_{IMF} = -1$ , and is in fair agreement with observed GMC mass distributions. As the radius of the window function is further decreased, the density fluctuations cross the barrier several times. Selecting the fluctuations for which the barrier is crossed for the last time, it is found that their mass spectrum is almost identical to the one inferred in Hennebelle & Chabrier (2008). The first type of structures, that is to say the fluctuations that cross the barrier for the first time, have been interpreted to represent giant molecular clouds, which are not themselves embedded in a larger self-gravitating cloud. The density fluctuations for which the barrier is crossed for the last time, represent prestellar core progenitors.

**4.1.4. Gravo-turbulent theory in a collapsing cloud.** As seen from Equation 34, the mass spectrum is a direct, linear, function of the density PDF. Therefore it is important to examine the prediction that are obtained for other density PDF, in particular the one, which develops during gravitational collapse as stated by Equation 10. The physical underlying idea is that as collapse proceeds new seeds to form self-gravitating objects develop.

We adopt a simplified but enlightening approach (Lee & Hennebelle 2018a). Following Equation 16, we simply write  $M \propto R^{2\eta+1}$ .  $\eta = 0$  corresponds to thermal or magnetic support whereas  $\eta \simeq 0.4 - 0.5$  is typical of turbulent support. Since  $\rho \propto M/R^3$ , we get  $\rho \propto M^{(2\eta-2)/(2\eta+1)}$ . Thus with Equations 34 and 10, and since both  $M$  and  $\rho$  are powerlaws

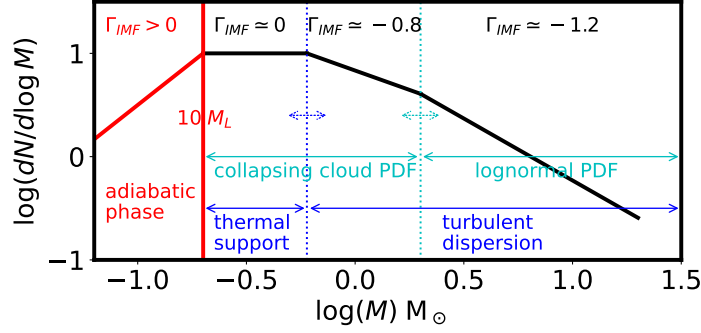


**Figure 3**

Schematic view of the gravo-turbulent theory predictions presented in Sects. 4.1.3, 4.1.4 and 4.2.3. From right to left, we distinguish four regions.  $\Gamma_{IMF} \simeq -1.2$  is obtained when the density PDF is lognormal and when at the scale of the mass reservoirs, turbulent dispersion dominates over thermal support.  $\Gamma_{IMF} \simeq -0.8$  is expected in regions where collapse has already occurred, implying that the density PDF is given by Equation 10, and turbulence still dominates over thermal support. On the other-hand,  $\Gamma_{IMF} \simeq 0$  is predicted to occur when thermal support dominates. Finally, when dust cooling becomes inefficient, objects of masses comparable to the mass of the FHSC,  $M_L$  are expected to form with a peak at about 10 times this value leading to  $\Gamma_{IMF} > 0$ . The transitions between the various regimes are not universal and depend on the physical conditions. For instance, if Mach numbers or column densities are very large, the regime  $\Gamma_{IMF} \simeq 0$  may not exist and a direct transition between  $\Gamma_{IMF} \simeq -0.8$  and  $\Gamma_{IMF} > 0$  may occur.

of  $R$ , it is easy to see that  $\mathcal{N}(M) \propto \sqrt{\rho} M^{-2}$  and therefore we obtain

$$\mathcal{N}(M) \propto M^{-\frac{1+5\eta}{1+2\eta}} = M^{-\frac{5\eta-13}{2\eta-4}}. \quad 36.$$

If, at the scale of the accretion reservoir, thermal or magnetic support are dominant  $\eta = 0$  and thus  $\mathcal{N}(M) \propto M^{-1}$  which implies  $\Gamma_{IMF} = 0$ . On the other hand, if turbulence is dominant at the scale of the accretion reservoir,  $\eta \simeq 0.5$  and  $\mathcal{N}(M) \propto M^{-7/4}$ , leading to  $\Gamma_{IMF} = -3/4$ . The transition between the two regimes is expected to occur roughly at the magneto-sonic scale, that is to say when  $3C_s^2 + V_a^2/2 \simeq V_{rms}^2$  (see Equation 16).

These predictions are major deviations from the Salpeter value,  $\Gamma_{IMF} = -1.33$  but they might explain lower values of  $|\Gamma_{IMF}|$  obtained for lower masses, or even the shallow slopes observed for dense starburst clusters (c.f. Fig. 1). As discussed in Section 5, both behaviours, i.e.  $\Gamma_{IMF} = 0$  and  $-3/4$  have been observed in numerical simulations. These considerations, therefore open the road for a non universal IMF made of universal regimes but whose domains of validity depend on both the support and the density PDF.

The value  $\Gamma_{IMF} = 0$ , obtained from thermal support at the scale of the accretion reservoir, is dominant, may constitute an effective peak for the IMF, evenso it would not lead to a real decline of the number of objects with masses. It is more accurately defined as a *plateau*. As discussed in Sections. 3.3.2 and 4.2.3, positive  $\Gamma_{IMF}$  will be induced by the adiabatic phase.

Figure 3 recaps the most important ideas presented in Sects. 4.1.3 and 4.1.4.

**4.1.5. Gravo-turbulence: the influence of filamentary geometry.** It has since long been established that filaments are ubiquitous in the ISM (Hacar et al. 2023). For instance many cores are observed to be lying inside larger scale filaments (Pineda et al. 2022).

The fragmentation of self-gravitating filaments as well as the possible role that this may have on the establishment of the IMF have thus been investigated. Inutsuka (2001) provided the first analytical calculation to predict the IMF from the fragmentation of a filament. His calculation is very similar to the classical approach of Press & Schechter (1974) except that it is applied to the filamentary geometry. The predicted mass spectrum is given by

$$\mathcal{N}(M) = \frac{dN}{dM} = -2 \frac{M_{line}}{M} \frac{\delta_c}{\sqrt{\pi}} \exp\left(-\frac{\delta_c^2}{2\sigma_M^2}\right) \frac{1}{\sigma_M^3} \frac{d\sigma_M^2}{dM} \propto \frac{M^{-3-n}}{\sigma_M^3}, \quad 37.$$

where  $M_{line}$  is the lineic mass of the filament and  $\sigma_M$  is the density variance. With  $n = -1.5$ , which is close to the Kolmogorov case, we have  $\mathcal{N}(M) \propto M^{-1.5}$  and therefore  $\Gamma_{IMF} = -0.5$ . Note that in the figure 1 of Inutsuka (2001) at early time an exponent close to  $\Gamma_{IMF} = -0.5$  is obtained but at later time an exponent closer to the expected Salpeter exponent appears. This is due to an evolution of the density variance,  $\sigma_M^2$ , which at later time is dominated by small scales because the development of gravitational instabilities has been taken into account into the calculation. Whether this may really lead to the formation of *new* structures is a matter of debate. Finally, let us also stress that since to obtain Equation 37, an integral is performed between  $M$  and  $\infty$ , this calculation represents groups of cores rather than individual cores, which request an integration between 0 and  $M$  (see for instance Equation 33).

More recently, Lee et al. (2017) have developed an analytical model in which the formalism presented in Section 4.1.3 is adapted to the filamentary geometry. The key feature of the model is that it considers a continuous transition for scales that are much smaller than the filament radius,  $R_f$  to scales larger than  $R_f$ . The criterion that density fluctuations must satisfied to collapse is based on the virial theorem as stated by Equation 16. The effect of an elongated geometry is accounted for by using an ellipsoidal model for the gravitational energy. Thermal, turbulent and magnetic support are all included. Both the CMF and the group of core distribution have been calculated (see figure 1 of Lee et al. 2017).

As expected, the CMF depends on the line mass and on the magnetic field strength. In particular, it is found that in the absence of magnetic field, filaments with high line mass fragment into many small cores. In the presence of a moderate magnetic field and for sufficiently high line mass, the CMF presents a peak around 0.5-1  $M_\odot$ . This however requires the Alfvénic Mach number to be on the order of 2-3. For lower values, no low-mass core would develop and the peak of the CMF would be at values of 10  $M_\odot$  or more. It should be stressed however that since the density PDF is assumed to be lognormal and collapse is not accounted for (see Section 4.1.4), the peak of the distribution is likely not physical. Importantly and interestingly, it is seen that the CMF in filaments with high line mass, turns out to present an exponent  $\Gamma_{IMF}$  that is fairly close to the Salpeter value. As discussed in Section 4.1.3, this is also what is inferred when filament geometry is not considered. It should therefore be stressed that whereas many stars appear to form in filaments, there is at this stage no clear evidence that the filamentary geometry is playing a particularly strong role regarding the IMF.

**4.1.6. Effect of MHD shock jump conditions.** The [Padoan & Nordlund \(2002\)](#) CMF/IMF model relies on MHD shocks, which are primarily responsible for setting up the value of  $\Gamma_{IMF}$  through the formation of compressed layers induced by ram pressure in a weakly magnetized medium. The magnetic field is assumed to be parallel to the compressed layer and therefore perpendicular to the gas velocity. The postshock density,  $\rho_1$ , the thickness of the layer,  $\lambda$ , and the postshock magnetic field,  $B_1$ , can all be related to the Alfvénic Mach numbers,  $\mathcal{M}_a = v/v_a$ , and preshocked quantities,  $\rho_0$  and  $B_0$  according to

$$\frac{\rho_1}{\rho_0} \simeq \mathcal{M}_a, \quad \frac{\lambda}{L} \simeq \mathcal{M}_a^{-1}, \quad \frac{B_1}{B_0} \simeq \mathcal{M}_a, \quad 38.$$

where  $L$  is the spatial extension of the incoming flow that gives rise to the shocked layer. Let us remind that for hydrodynamical isothermal shocks,  $\rho_1/\rho_0 \propto \mathcal{M}^2$ ,  $L/\lambda \propto \mathcal{M}^2$ . The dependence on  $\mathcal{M}_a$  instead of  $\mathcal{M}^2$  is due to the magnetic pressure which is proportional to  $B^2$ .

The typical mass of this perturbation is given by  $M \simeq \rho_1 \lambda^3$  leading to

$$\begin{aligned} M &\simeq \rho_0 L^3 \mathcal{M}_a^{-2} \text{ MHD,} \\ M &\simeq \rho_0 L^3 \mathcal{M}^{-4} \text{ HYDRO} \end{aligned} \quad 39.$$

As the flow is turbulent, the velocity distribution depends on the scale and  $v \simeq L^{(n-3)/2}$ . With Equation (39), one infers  $M \propto (L/L_0)^a$  where  $L_0$  is the integral scale and  $a = 6 - n$  in MHD or  $a = 9 - 2n$  in hydro. To get a mass spectrum, it is further assumed that the number of cores,  $N(L)$  at scale  $L$ , is proportional to  $L^{-3}$ . These two relations lead to  $\Gamma_{IMF} = -3/a$ . For  $n = 3.8$ , one gets  $\Gamma_{IMF} \simeq -1.36$  in MHD and  $\Gamma_{IMF} \simeq -2.14$  in hydro.

In a second step, a lognormal distribution of Jeans masses within the clumps is envisioned and the mass spectrum is therefore multiplied by a distribution of Jeans masses,  $\int_0^M p(M_J) dM_J$ . The shape of the final mass spectrum is very similar to the observed IMF as seen for example in the Figure 1 of [Padoan & Nordlund \(2002\)](#).

Note that this theory presents two significant difficulties. First of all, Equation 38 implies that in the densest regions where dense cores form, the magnetic field strength is proportional to the density and this is not in good agreement with what is observed both in numerical simulations and in observations. As recalled in Section 3.4, in numerical simulations it is usually found that at high densities the trend  $B \propto \sqrt{\rho}$  is inferred. Second of all, the theory predicts that in the hydro case  $\Gamma_{IMF} \simeq -2$  and this is not compatible with hydrodynamical simulations as discussed in Section 5.

## 4.2. How to explain the characteristic mass of stars?

The existence of a relatively well defined peak of the IMF is at first sight surprising because the ISM presents a wide range of processes and physical conditions. Below we review the various ideas which have been proposed and briefly present the arguments in favor or against their validity.

**4.2.1. Possible role of the Jeans length in setting a peak.** The Jeans length ([Jeans 1902](#)) has often been envisaged to be playing a significant role regarding cloud fragmentation and even possibly to be at the origin of the peak of the IMF. One important difficulty however is that it presents a relatively strong dependence on density and temperature since as shown by Equation 12,  $M_{jeans} \propto T^{3/2} \rho^{-1/2}$ . Since both temperature and density are observed

to vary substantially through star forming regions, this is in apparent contradiction with the apparent universality of the IMF but various propositions have been made to combine Jeans mass considerations with other physical arguments.

Larson (2005) has proposed that the transition between the molecular cooling and the dust cooling leads favors fragmentation at the density at which this transition occurs. Indeed, the effective adiabatic index induced by molecular cooling is about  $\Gamma_{\text{ad}} \simeq 0.7$  whereas dust cooling leads to  $\Gamma_{\text{ad}} \simeq 1.1$ . Since the transition between the two cooling regimes occurs at about  $10^5 \text{ cm}^{-3}$ , the Jeans mass would be compatible with a peak around 0.3-0.5  $M_{\odot}$  (see also Elmegreen et al. (2008)). Hennebelle & Chabrier (2009) have developed an analytical model for the CMF in which the two cooling regimes are taken into account but could not identify the corresponding peak. This also cannot be a *general* explanation for the IMF, because some very-dense clusters like Orion have an essentially normal-looking IMF peak, but must have formed in conditions orders of magnitude denser than the transition density (Krumholz 2014). Nevertheless it cannot be discarded *a priori* as an explanation for the IMF in less-dense, more-typical Solar neighborhood clouds. This scenario has been explored in simulations and the result will be discussed in Section 5.2.3.

The gravo-turbulent theories (Padoan et al. 1997; Hennebelle & Chabrier 2008) identify a peak in the reservoir distribution when they assume a lognormal density PDF, that is to say assume that a density and therefore a Jeans length is dominating the distribution. Hennebelle & Chabrier (2008) found that the peak of the reservoir mass function is given by  $M_J^0/\mathcal{M}^2$ , where  $M_J^0$  is the Jeans mass of the mean density and  $\mathcal{M}$  the Mach number. In principle, this must lead to some significant variations of the peak since large variations of density and velocity dispersion are observed between the clumps. However, it has been proposed that due to Larson relations (Larson 1981), some compensations may occur leading to less variability. Indeed, the CO clumps are observed to present a scaling  $M \propto R^2$  or equivalently  $\rho \propto R^{-1}$  and  $\delta v \propto R^{0.4}$ . This would lead to  $M_J^0/\mathcal{M}^2 \propto R^{0.3} \propto M^{0.15}$ . The latter relation is a shallow dependence, which could therefore possibly explain a weak variation of the peak of the IMF from regions to regions. There are however two main caveats. First there are large deviations around Larsons relations which would result in large variations of the peak and second at high density the PDF is not lognormal any more (see Section 4.1.4) and therefore these considerations would become invalid.

**4.2.2. Protostellar heating.** When a star forms, the accretion luminosity heats the gas around and increases the temperature, therefore increasing the Jeans mass around the protostar. It has been proposed by Bate (2009), Krumholz (2011) and Guszejnov et al. (2016) that this leads to a very shallow dependence of the Jeans mass into the density and therefore may constitute a possible way to explain the characteristic mass of stars. Below we follow the arguments presented in Krumholz (2015).

Let us consider a protostar of luminosity  $L$ , at a distance  $r$ , we have the relation

$$L \simeq 4\pi\sigma_{sb}r^2T^4, \quad 40.$$

where we remind that  $\sigma_{sb}$  is the Stefan-Boltzmann constant. The idea is now to compare the Jeans mass,  $M_J \propto C_s^3\rho^{-1/2}$  with the mass,  $M \propto \rho r^3$ , enclosed in the radius  $r$ . If these two masses are comparable, fragmentation is likely suppressed and therefore the mass should be accreted in a single object. Writing  $M_J \simeq M$  and using Equation 40, we get that  $M \propto L^{3/10}\rho^{-1/5}$ . Next it is assumed that the luminosity,  $L$  is the accretion luminosity and thus  $L \propto \dot{M}$ , with the constant of proportionality set by the condition for deuterium

burning (Equation 24), and  $\dot{M} \simeq M/\tau_{ff} \propto M\sqrt{\rho}$ . Thus this leads to  $M \propto \rho^{-1/14}$ . The full expression obtained by (Krumholz 2015) is (see his equation 13.38)

$$M = 0.3M_{\odot} \left( \frac{n}{100 \text{ cm}^{-3}} \right)^{-1/14}. \quad 41.$$

As can be seen, this mass has a very shallow dependence in gas density and therefore little variation is expected across environments. Moreover its value is very close to the estimated peak of the IMF. The more-detailed semi-analytic radiative transfer calculation by Krumholz (2011) gives a mass scale approximated by (see Figure 5 of Krumholz 2011)

$$M \approx 0.03M_{\odot} \left( \frac{P}{10^{10} k_B \text{ K cm}^{-3}} \right)^{-0.28} (Z_d)^{-0.22}, \quad 42.$$

where  $P$  is the confining pressure of the clump and  $Z_d$  is the dust opacity parameter. This is significantly more sensitive to ambient conditions than the corresponding analytic approximation, but still less so than the Jeans mass.

A possible difficulty of this theory is that the density or pressure that is involved in the mass estimate is not very clearly defined. When a protostar has formed, the density distribution around it, is likely an  $r^{-2}$  powerlaw and in this configuration, the Jeans mass is not uniquely determined. Also when radiation starts, the reservoir is already globally collapsing and it requires a strong heating to stop. As discussed in Section 5.5, numerical studies exploring this scenario have arrived at conflicting results.

**4.2.3. First hydrostatic core and tidal screening.** Lee & Hennebelle (2018b) and Hennebelle et al. (2019) have proposed that the peak of the IMF may be related to the mass of the first hydrostatic core (Section 3.1.3). The proposed mechanism works in three steps. First, the formation of the first hydrostatic core signs the transition from an isothermal to an adiabatic equation of state. The latter suppresses any further fragmentation and essentially stops the collapse. Second, the gas piles-up until the central temperature becomes sufficiently high for  $\text{H}_2$  to dissociate. At this point the mass of the first hydrostatic core is about  $0.03 M_{\odot}$  and this constitutes the minimal mass that needs to be accumulated in order to produce a protostar. Third, the first hydrostatic core is surrounded by a collapsing, nearly isothermal envelop and can further accrete and grow. The surrounding gas can however also fragment and produce new objects instead of being accreted. However, both the first hydrostatic core and the collapsing envelope (which typically has a profil  $\rho \propto r^{-2}$ ) exert tidal forcing on the surrounding medium and this stabilizes the gas around against fragmentation. Hennebelle et al. (2019) developed a model which predicts that this results in a central object that typically has a mass of about 10 times the mass of the first hydrostatic core, which is about  $10 \times 0.03 M_{\odot} = 0.3 M_{\odot}$ . The model considers concentric shells around the first hydrostatic core and compute the probability to find self-gravitating density fluctuations with a mass at least equal to the mass of the first hydrostatic core. The mass contained in the radius for which the probability to find  $n$  density fluctuations, is then computed.

A simple model has been proposed by Colman & Teyssier (2020). The argument is as follows. Let us consider a central point mass such as a first hydrostatic core and let  $M_{FHSC}$  be its mass. As collapse is proceeding this object is surrounded by a density envelope  $\rho_{env} = Ar^{-2}$ , where  $A$  is a constant. A simple condition for fragmentation to occur is that the self-gravity of the envelope is lower than the tidal force induced by the



first hydrostatic core and this leads to  $2GM_{FHSC}r_{tidal}^{-3} = 4\pi/3G\rho_{env}$ . We thus obtain

$$r_{tidal} = \frac{6M_{FHSC}}{4\pi A}. \quad 43.$$

The gaseous mass enclosed within  $r_{tidal}$  is thus

$$M_{tidal} = \int_0^{r_{tidal}} 4\pi r^2 dr = 4\pi A r_{tidal} = 6 \times M_{FHSC}. \quad 44.$$

Assuming that the total mass,  $M_{tidal}$ , is accreted onto the central first hydrostatic core, we thus obtained that the peak of the IMF would be about  $7 \times M_{FHSC} \simeq 0.2 M_{\odot}$ . Remarkably enough the tidal mass does not depend on the constant  $A$  and this implies that it is likely relatively insensitive to the environmental conditions.

We stress that this theory to explain the peak of the IMF does not primarily rely on Jeans mass consideration but rather on the mass of the FHSC which as discussed earlier depends on the detailed microphysics of the ISM (see Equations 5 and 6) and more particularly on the dust opacity and of the  $H_2$  physics. Moreover the dependence on the metallicity is expected to be very shallow (see Equations 5).

Altogether, the tidal screening theory appears to weakly depend on large scale conditions and ISM composition which makes it a good candidate to explain the relative universality of the peak of the stellar initial mass function.

## 5. Current state of the art in numerical simulations - testing the theories

A broad set of simulations have been performed with increasing accuracy, both regarding the physics and the numerical resolution. We discuss here the various types of simulations from the simplest, in terms of physical processes, to the most complete calculations. Whenever possible, we make the link with the analytical models discussed in the previous section.

### 5.1. Numerical algorithms and caveats

Before discussing the results of the various simulations we need to stress some of the most important limits and numerical uncertainties that must be addressed. For a description of the numerical techniques themselves, which are beyond the scope of the present paper we refer to other, more-comprehensive discussions [Teyssier & Commerçon \(2019\)](#) and [Grudić et al. \(2021\)](#). We stress that substantially diverse codes, ranging from Eulerian adaptive mesh refinement algorithm to Lagrangian smoothed particle hydrodynamics, moving mesh, and mesh-free Godunov-type codes are now employed in the star formation community. Comparisons between different codes have generally found fair agreement in hydrodynamics setups with simple EOS, provided sufficient resolution (e.g. [Commerçon et al. 2008](#); [Ferrerath et al. 2010](#)). However, further careful code comparisons will be useful as complex, multi-physics simulation setups with subgrid feedback prescriptions become more common: the impact of the further numerical choices required will deserve some investigation.

In the present context, two aspects of the simulations require a particular attention. First, and as it is most often the case, the issue of numerical resolution must be carefully addressed. This is most notably true for the question of the peak of the IMF as it is unavoidable that given the number of resolution elements (e.g. [Bate et al. 1995](#); [Truelove et al. 1997](#); [Grudić et al. 2021](#)), there is a minimum mass which can be described with a given specific algorithm. It is therefore necessary to perform systematic convergence tests and



to obtain resolution independent results to study the IMF with numerical simulations. It must in particular be stressed that in simulations that do not include physical processes (as discussed in Section 4.2) able to generate a peak in the sink particle distributions (aiming at representing the IMF), a numerical peak due to finite spatial resolution nevertheless appears and it is fundamental to distinguish between *physical* and *numerical* peaks. It should also be made clear that getting self-consistently a whole IMF in a single simulation remains very challenging. Indeed forming simultaneously very massive stars, say of  $100 M_{\odot}$ , and in the same time resolving objects of  $10^{-2} M_{\odot}$  like the FHSC, requires resolving spatial or mass scales that differ by at least 4 to 5 orders of magnitude. Obviously dealing with the corresponding timesteps is a significant part of this challenge, in particular because processes like non-ideal MHD, jets and winds lead to severe constraints.

The second key issue is the usage of the Lagrangian sink particles that model the accretion, stellar evolution, and feedback processes occurring below the resolution limit (Bate & Burkert 1997; Krumholz et al. 2004; Hubber et al. 2013; Bleuler & Teyssier 2014; Grudić et al. 2021). These methods inevitably introduce ad-hoc constructs into the simulation that do not correspond to physical source terms and are not guaranteed *a priori* to produce numerically-converged results. This is not ideal, but will remain necessary until it becomes possible to resolve stellar radii in star cluster calculations. The choice of the numerical parameters can potentially have decisive effects on the results, so it is important to check that *i*) the prescription chosen can at least robustly model exactly-known point-mass accretion solutions (see Section 3.6), and *ii*) the IMF produced is not affected by specific choices of numerical parameters.

## 5.2. Barotropic equation of state and hydrodynamical simulations

Historically the first simulations that have been carried out to infer a statistical distribution of stars (or more accurately of sink particles) were hydrodynamical and were either purely isothermal (Klessen 2001) or have been using a barotropic equation of state (eos) meaning that the pressure is a (often piece-wise) prescribed function of the density  $P = K_i \rho^{\Gamma_{ad,i}}$  for  $\rho_i < \rho < \rho_{i+1}$  (Bate et al. 2003). This constitutes an easy way to mimic cooling and radiative process. Various prescriptions have been used, depending which physics was under investigation. Here we make the important distinction between *soft* and *hard* eos. The former corresponds to an effective adiabatic index,  $\Gamma_{ad,i} < 4/3$ . As recalled in Sec. 3.3.2,  $\Gamma_{ad} = 4/3$  is indeed a critical value. Collapse is completely halted for  $\Gamma_{ad} > 4/3$ .

**5.2.1. Isothermal-like calculations.** Many isothermal, or effectively isothermal hydrodynamics IMF calculations have been performed. Here we report the results of several calculations that are either strictly isothermal or which are, for the aspect discussed in this section, equivalent to an isothermal calculation.

Girichidis et al. (2011) performed a series of calculations of  $100 M_{\odot}$  collapsing clouds with various initial density profiles. When the cloud has an initially-flat density profile (top hat or Bonnor-Ebert sphere), the sink mass spectra that develop, tend to present a peak, typically located at a mass of a few  $10^{-2} M_{\odot}$ , and for larger masses, a power-law behaviour. The exponent of this latter has not been systematically measured. It is possibly compatible with  $\Gamma_{IMF} = -1.35$  but for several cases, it appears to be in better agreement with  $\Gamma_{IMF} = -1$  or possibly even larger values. These results are in good agreement with the ones presented in Ballesteros-Paredes et al. (2015) where  $1000 M_{\odot}$  clouds of various

size and Mach numbers have been investigated. They also found a value of  $\Gamma_{IMF} \simeq -1$ .

Guszejnov et al. (2018) and Lee & Hennebelle (2018b) also studied the collapse of massive clumps and carried out runs that are strictly isothermal. The results were qualitatively similar to Girichidis et al. (2011) and Ballesteros-Paredes et al. (2015), but they performed systematic numerical convergence tests and found that the peaks of the stellar distributions shifted toward smaller mass when the numerical resolution is improved, a result first noticed by Martel et al. (2006) using particle splitting in SPH. Both studies have therefore concluded that in isothermal hydrodynamics, the peak of the sink mass spectrum is *entirely numerical*, and not physical. In principle, this result could be due to an error in the sink particle implementation, rather than the actual mass spectrum that would occur physically, but the fact that this is seen in SPH, AMR, and MFM implementations suggests that it is robust. Physically, this result may be understood by the tendency of isothermal, self-gravitating filaments to form spontaneously in turbulent flows, and then to collapse to infinite density synchronously along their length without fragmenting (Inutsuka & Miyama 1992). Isothermal disks that form would also be prone to catastrophic fragmentation (Kratte et al. 2010). The existence of a well-defined, converged mass spectrum from self-gravitating, isothermal turbulence is difficult to rule out *a priori*, but it has yet to be demonstrated in numerical models (except Gong & Ostriker 2015, where numerical convergence for cores is claimed). This is a serious problem for all analytic models that attempt to explain the IMF in terms of isothermal, self-gravitating hydrodynamics (c.f. Section 4)

Lee & Hennebelle (2018a) have explored the influence of initial conditions performing a series of calculations for which the gas remains isothermal below  $\simeq 10^{10} \text{ cm}^{-3}$ . In particular the initial density of their 1000  $M_{\odot}$  runs is varied by 4 orders of magnitude, keeping the ratio of kinetic over gravitational energy constant. This implies that in these runs, the thermal over gravitational energy is varied by a factor 25 and the Mach number by about a factor of 10, between 7 and 50. Figure 4 portrays the results. An important change of behaviour arises for a Mach number of about 10 (which corresponds to run B in figure 4). Above this value, all runs display a mass spectrum with  $\Gamma_{IMF}$  of about -3/4 to -1. However for a Mach number of  $\simeq 7$ , the mass spectrum has been found to be extremely flat,  $\Gamma_{IMF} \simeq 0$ . Such *plateau* IMF, which have also been observed in other calculations (e.g. Bonnell et al. 2006; Jones & Bate 2018)<sup>2</sup> are naturally explained by the gravo-turbulent theory applied to a collapsing cloud PDF as presented in Section 4.1.4 and a quantitative comparison is presented in figure 8 of Lee & Hennebelle (2018a). The change of  $\Gamma_{IMF}$  from 0 to  $\simeq -1$  comes from the fact that at low Mach number, the thermal term dominates the support of the mass reservoirs, whereas for high Mach numbers the dominant support is due to turbulence. This latter, unlike the former, is scale dependent. Another important quantity which can be inferred from the simulations is the accretion rate onto the stars/sink particles. In Figure 5 of Lee & Hennebelle (2018a) a comparison is made between the mass of the sinks and the accretion time measured in the simulations and predicted by the gravo-turbulent theory and a good agreement is found.

Interestingly, Ballesteros-Paredes et al. (2015) have been interpreting their own results, that is to say their inference of  $\Gamma_{IMF} \simeq -1$  as a consequence of competitive accretion as described in section 4.1.1. They stress that the basic assumption of competitive accretion,

---

<sup>2</sup>The value of  $\Gamma_{IMF} \simeq 0$  is also commonly reported in simulations attempting to model primordial stars, (e.g. Klessen & Glover 2023) where a change with high Mach number is also reported, see for instance Figure 11 of Chon et al. (2022).

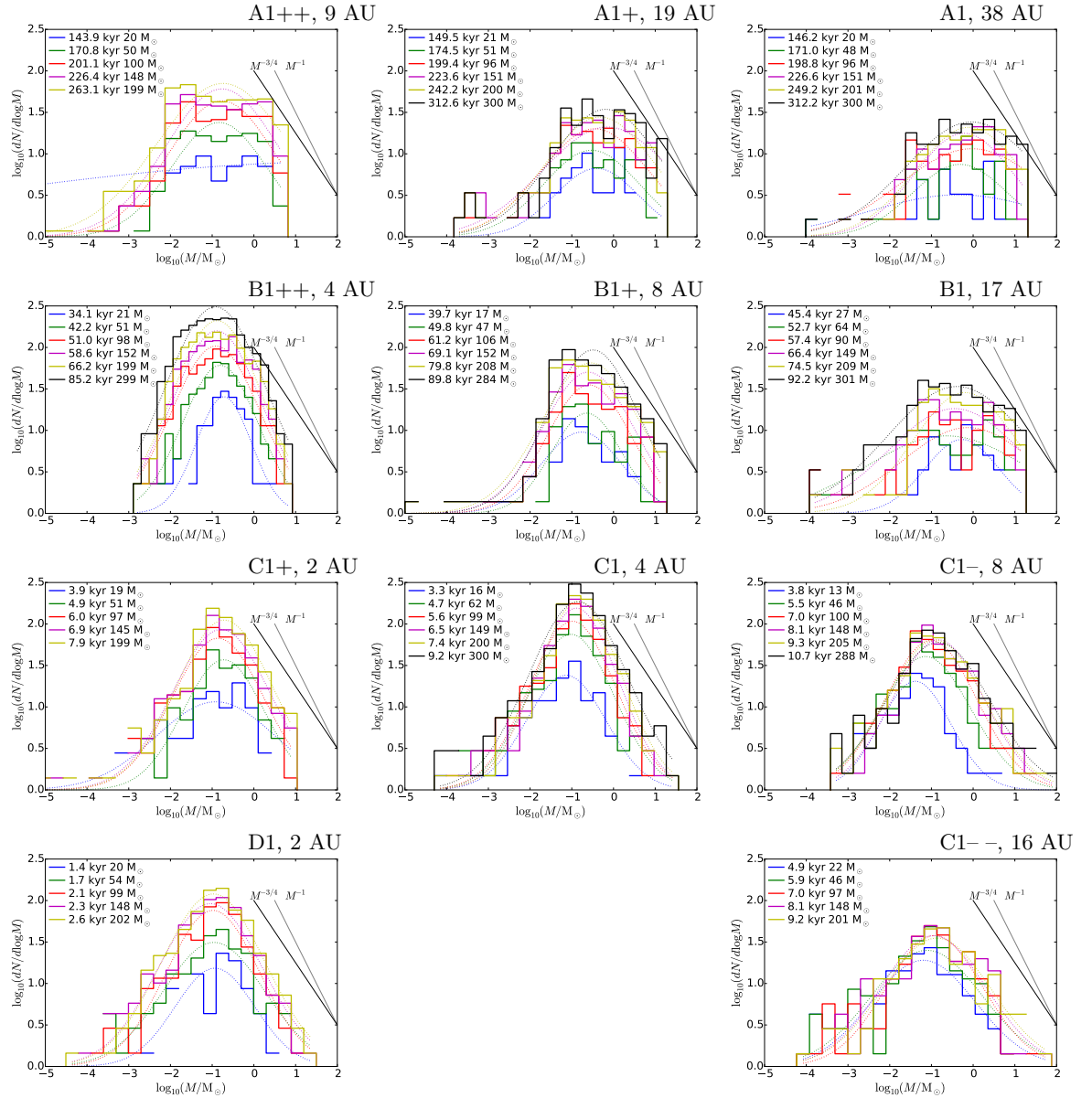


**Figure 4**

A series of numerical simulations of a  $1000 M_{\odot}$  clump from Lee & Hennebelle (2018a). Runs A, B, C and D correspond to four initial densities (respectively  $8 \times 10^4$ ,  $9 \times 10^5$ ,  $6 \times 10^7$ ,  $5 \times 10^8 \text{ cm}^{-3}$ ) and several numerical resolutions. Run A presents a plateau with  $\Gamma_{IMF} \simeq 0$ , Runs C and D show a peak at about  $0.1 M_{\odot}$  which is independent of numerical resolution and a powerlaw regime with  $\Gamma_{IMF} \simeq -3/4 - 1$ . Run B is intermediate between runs A and C and presents the two regimes of  $\Gamma_{IMF}$ . Reproduced with the permission of A&A.

namely  $\dot{M} \propto M^\alpha$ ,  $\alpha = 2$  is not observed in their simulations where  $\alpha$  ranges from 0 to 0.8-1 (see their Figure 2). They however argue that competitive accretion occurs locally rather than globally and correcting for the local environment they then infer  $\alpha \simeq 2$ . This result may suggest that both gravo-turbulent fragmentation and competitive accretion may well be operating at the same time. Within a reservoir in which several stars have formed, there may possibly be, at least some, *competitive accretion*, between the stars. Such a scenario is compatible with the results reported by [Smith et al. \(2008\)](#) where the usage of the SPH Lagrangian scheme allows a full tracking of the mass. Identifying the accretion reservoir where the sink particles formed, they studied the correlation between the sink and the reservoir masses. They concluded that a very good correlation between the two is found up to about 3-5 local freefall times (as revealed by their Figure 10). At later time, the correlation persists but becomes progressively less tight (see their Figure 9).

Generally speaking, determining the correspondance between a specific gas reservoir and a star is not an easy task. It has often been considered that the prestellar cores (see Section 2.3) should correspond to the reservoir out of which stars built their mass, but detailed studies have found that the correspondance between simply defined reservoirs, as considered in gravo-turbulent theories, and the mass effectively accreted by stars may be imperfect ([Pelkonen et al. 2021](#)) as only a fraction of the material ends up in the sink. One possibility is that this is due to the complex velocity field not taken into the reservoir definition and to the fact that most of the core mass is located in their outskirt. Indeed studies which have investigated the importance of geometry, the tidal field, and surface terms of the virial theorem, which are usually not accounted for, have found that their contributions are significant ([Ballesteros-Paredes 2006](#); [Dib et al. 2007](#); [Hennebelle et al. 2019](#)). It is however likely the case, that the statistics inferred for the idealised reservoirs, or say the cores, may actually be close to the statistics that would be inferred for the actual reservoirs because both populations should indeed be closely related. This clearly requires future investigations.

To summarize, the mass spectra in isothermal calculations of massive collapsing clumps tends to predict various asymptotic values for  $\Gamma_{IMF}$ , which depending on the initial conditions can be equal to 0 or  $\simeq -0.8$  to  $-1$ . Note that in observations, the range of mass for which  $\Gamma_{IMF} \simeq 0$  is reported appears to be quite narrow (see Figure 1). Therefore it is surprising that prominent *plateau* IMF, i.e.  $\Gamma_{IMF} \simeq 0$  ranging up to masses of several  $M_\odot$ , are found for initial conditions that do not appear to be unusual in the ISM (i.e. run A of Figure 4). As discussed in Section 5.7, it is likely that protostellar jets and outflows may be solving this apparent contradiction.

Finally, we reiterate that the peak of the mass spectrum, i.e. the existence of a mass range where  $\Gamma_{IMF} > 0$ , obtained in isothermal calculations is likely numerical.

**5.2.2. Influence of a hard eos,  $\Gamma_{ad} > 4/3$ .** As discussed in Section 3.1.2, at high density (i.e. above  $10^{10} \text{ cm}^{-3}$ ) transport of dust emission becomes inefficient and the eos becomes adiabatic. Therefore several works have employed an eos that is isothermal at low densities and adiabatic at high densities (e.g. [Bate et al. 2003](#); [Bonnell et al. 2011](#); [Bate 2012](#)). For instance, [Bate et al. \(2003\)](#) employed  $\Gamma_{ad} = 1$  for  $\rho < \rho_{ad} = 10^{-13} \text{ g cm}^{-3}$  and  $\Gamma_{ad} = 7/5$  for larger  $\rho$ .

[Lee & Hennebelle \(2018b\)](#) have performed a series of calculations to investigate the role of the eos on the peak of the IMF. Both the values of  $\Gamma_{ad}$  and  $\rho_{ad}$  have been varied. Several important conclusions have been inferred. First of all, numerical convergence of the stellar

mass spectrum can be established when such an eos is used as revealed by Figure 4<sup>3</sup>. This is a major difference with the case of an isothermal eos for instance. Second of all, the position of the peak of the IMF depends on both  $\Gamma_{ad}$  and  $\rho_{ad}$ . Since these values can be associated to a specific value of  $M_{FHSC}$  (see Equation 6), it is possible to investigate the dependence on the IMF peak onto  $M_{FHSC}$  by varying the values of  $\Gamma_{ad}$  and  $\rho_{ad}$ . Lee & Hennebelle (2018b) found that  $M_{peak} \simeq 10 \times M_{FHSC}$  as revealed by their Figure 8. This finding has led to the model exposed in Section 4.2.3. In essence due to the hard eos, the gas piles up until the central mass equals  $M_{FHSC}$ , providing a robust minimum mass for the stars that form. The factor of  $\simeq 10$  between  $M_{peak}$  and  $M_{FHSC}$  is less straightforward to understand and according to the model of Hennebelle et al. (2019) is due to the tidal forces, which in the neighbourhood of an existing self-gravitating object prevent further fragmentation and favor further accretion into the object. Colman & Teyssier (2020) conducted a systematic investigation of the influence of tidal forces in the neighbourhood of their sink particles at their birth, by computing the mass of gas within the regions where tidal forces prevent the formation of new fragments (see their figures 15 and 16). The mass distribution of these tidally protected gas reservoirs has been found to be very close to the sink particle distribution seemingly suggesting that the two are very closely related.

The proposed origin for the peak of the IMF, which is due to *i*) the mass of the first hydrostatic core and *ii*) the stabilizing effect of the tidal forces that prevent close fragmentation, leading to further accretion onto the existing object, is an appealing scenario because it does not depend very sensitively on large scale initial conditions, as indeed verified by Lee & Hennebelle (2018a) and therefore it predicts a relatively universal peak for the IMF<sup>4</sup>. Let us stress that since these calculations employed an eos, it is necessary for full self-consistency, to perform calculations that properly treat radiation as discussed in Section 5.5.

**5.2.3. Influence of a soft eos,  $\Gamma_{ad} < 4/3$ .** As recalled in Section 4.2.1, Larson (2005) proposed that the peak of the IMF could be determined by the Jeans mass of the density ( $\simeq 10^5 \text{ cm}^{-3}$ ) at which the effective eos transitions from  $\Gamma_{ad} \simeq 0.7$  to  $\Gamma_{ad} \simeq 1.1$  due to the transition from molecular cooling to dust cooling. This picture has been investigated by Jappsen et al. (2005) (see also Bonnell et al. 2006), who have presented a comprehensive set of numerical simulations with such an eos. In particular, they varied the density  $n_{ad}$  at which the transition between the two values of  $\Gamma_{ad}$  occurs. They found that, indeed the median stellar mass (expected to be close to the peak mass), is proportional to  $\simeq n_{ad}^{-0.5}$  (see their Figure 6). However these results are somewhat inconclusive in light of the possible convergence issues demonstrated in the works discussed in § 5.2.1; Jappsen et al. (2005) did survey a variety of mass resolutions, but did not explicitly demonstrate robustness to resolution in a controlled comparison. In fact, their Table 1 indicates that higher-resolution simulations do tend to produce more objects at lower final SFE, consistent with results in Section 5.2.1. This scenario should thus be revisited in light of the findings of subsequent studies, particularly regarding the issue of numerical convergence.

<sup>3</sup>Note that the convergence regarding the smallest objects that form may not have been reached for run A for which the best resolution is only of 9 AU

<sup>4</sup>In simulations for which a plateau IMF develops, the FHSC leads to a lower mass limit rather than a peak.

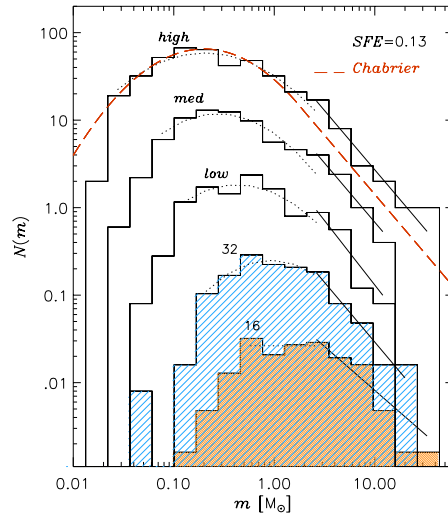


**Figure 5**

IMF formed within magnetized isothermal collapse calculations of a turbulent box with different numerical resolution from [Haugbølle et al. \(2018\)](#). Note that the relative bin heights are shifted for visualization purposes. Reproduced with the permission of the authors.

### 5.3. The role of the magnetic field

We now discuss the role magnetic field may have in shaping the IMF. We restrict the discussion to isothermal or barotropic runs and postpone the discussion of magnetic field in the presence of radiative transfer to the Section 5.5 or in the presence of jets to the Section 5.7.

[Haugbølle et al. \(2018\)](#) have performed isothermal MHD runs in a driven periodic box setup with side length 4pc containing  $3000 M_{\odot}$  (if the inherently scale-free system is placed on scaling relations corresponding to  $C_s \sim 0.19 \text{ km s}^{-1}$ ). The Mach number is about 10 and the Alfvénic Mach number is equal to 4. In terms of magnetic field strength this would correspond to a field of about  $7 \mu\text{G}$  at a density of about  $700 \text{ cm}^{-3}$ . The numerical resolution is systematically varied from 800 to 50 AU. At the highest resolution, a relatively good agreement with the Chabrier’s IMF (see figure 5) is obtained except around  $1\text{-}3 M_{\odot}$ . As the resolution is increased from 800 AU to 50 AU, the peak of the IMF is observed to shift to lower mass (as it is also the case for instance in [Guszejnov et al. 2018](#)). The question as to whether numerical convergence has been reached in these simulations is therefore critical. The authors show that as resolution increases the position of the peak keeps increasing but seems to decrease less rapidly with resolution, suggesting some degree of convergence or robustness to numerical resolution. These authors paid particular attention to the particulars of the sink-particle implementation, finding that a fine-tuned accretion algorithm was essential to avoid the formation of spurious sink particles. If this result proves to be robust, it will be essential to understand why this is happening whereas hydrodynamical simulations do not seem to show sign of convergence. After all, ideal MHD does not introduce any particular scale in the problem that would explain why recursive fragmentation stops to occur at some scales or some density. On the other hand, the presence of magnetic fields

could quite conceivably alter the dynamics of filamentary collapse (e.g. Lee et al. 2017). Haugbølle et al. (2018) also performed runs with 4 different total masses, corresponding to 4 virial parameters. They find that the shape of the IMF shifts to lower mass as the virial parameter decreases. This is qualitatively in good agreement with the gravo-turbulent theories since the mean Jeans mass is lower in the simulations that contain more mass.

Lee & Hennebelle (2019) have carried out MHD barotropic simulations of a collapsing  $1000 M_{\odot}$  virialised cloud with a maximum spatial resolution of about 4 AU. Two different initial densities have been explored, respectively  $8 \times 10^4$  (diffuse) and  $6 \times 10^7 \text{ cm}^{-3}$  (dense). The initial Alfvénic Mach number has been varied from 11 to  $\simeq 0.9$  for the dense clump whereas for the diffuse one it has been chosen to 2.75. For the dense clump initial condition, the IMF presents a marked peak at about  $\simeq 0.1 M_{\odot}$  whereas at higher mass the IMF exhibits a powerlaw with an exponent  $\Gamma_{IMF} \simeq -1$ . This is the case for the Alfvénic Mach numbers, which have been explored. Some possible variations for the lower mass objects are possibly observed but altogether for the dense initial conditions, the magnetic field appears to have a modest influence on the IMF. The physical reason may be that the magnetic field strength is observed to converge at densities larger than about  $10^9 \text{ cm}^{-3}$  toward values which are nearly independent of the initial magnetisation. For the diffuse clump, the IMF, even in the hydrodynamical case, is such that  $\Gamma_{IMF} \simeq 0$ , which as explained in Section 4.1.4 arises when the thermal support dominates at the scale of mass reservoirs. In this context, magnetic field does not significantly alter the mass spectrum since the Alfvén speed, as the sound speed, is roughly scale independent (see Section 3.4). Interestingly however, there are less low mass objects in the MHD than in the hydrodynamical runs indicating that in this configuration, magnetic field reduces fragmentation.

Guszejnov et al. (2020) have performed a series of scale-free, magnetized isothermal GMC simulations with the Meshless Finite Mass method, surveying a wide range of Mach numbers ( $\mathcal{M} \sim 5 - 50$ ), corresponding to masses ranging from  $\sim 10^3 - 10^6 M_{\odot}$  for clouds on Larson’s relations. They also surveyed a range of  $\mu$  values from more than 10 to about 1 with 4 being the standard value, and a range of virial parameters  $\alpha \sim 0.5 - 4$ . Several trends are inferred. For large masses they get  $\Gamma_{IMF} \simeq -1$  or steeper whereas at low masses,  $\Gamma_{IMF} \simeq 0$ . They surveyed numerical resolution systematically and did not claim strong convergence of the overall mass spectrum, as finer mass resolutions did always result in more low-mass sinks. But they did find that *mass-weighted* quantiles of the IMF could be remarkably well-converged over many decades in mass resolution, in contrast to their previous isothermal hydrodynamics results which did not converge in any sense (c.f. Section 5.2.1). While also finding an IMF from isothermal MHD with some degree of robustness to resolution like Haugbølle et al. (2018), they did *not* concur that this formula is sufficient to explain the IMF: their models, when scaled to real clouds, predicted stellar mass quantiles an order-of-magnitude too large. They therefore concluded that only additional physics capable of *reducing* stellar masses – such as protostellar outflows – are also necessary in these conditions (see Section 5.7).

#### 5.4. How turbulence and numerical setup influence the IMF

As mentioned above, two main numerical setups have been traditionally used to compute the IMF, namely isolated turbulent collapsing clumps (e.g. Bate et al. 2003; Ballesteros-Paredes et al. 2015; Lee & Hennebelle 2018a) and periodic boxes in which turbulence is driven (e.g. Haugbølle et al. 2018; Mathew et al. 2023). In the former configuration, turbu-



lence is initially imprinted and is not further driven. Lee & Hennebelle (2018a) have varied the initial virial parameter (their figure 7) between 1.5 and 0.1 and found that unless its value is smaller than  $\simeq 0.3$ , the influence of its variation remains limited. In particular,  $\Gamma_{IMF}$  is not significantly affected and remain close to -0.8 to -1. The values of  $\Gamma_{IMF}$  reported in the periodic boxes tend to be steeper and closer to -1.3. For instance, figure 5 (Haugbølle et al. 2018) reveals that the high mass part of the stellar distribution, between  $\simeq 2$  and  $10 M_{\odot}$  appears to be compatible with  $\Gamma_{IMF} \simeq -1.3$ . Similar trends may be found in the work of Mathew et al. (2023), where turbulence driving is also performed and values of  $\Gamma_{IMF} \simeq -1.3$  are also seemingly obtained (their figure 7). The difference between the two configurations clearly appears in figure 16 of Guszejnov et al. (2022) where periodic boxes with and without turbulent driving, as well as collapsing clouds have been investigated. All cases have  $\Gamma_{IMF} \simeq -1$  except the turbulent driven simulation for which  $\Gamma_{IMF} \simeq -1.3$ .

The reason of these differences is presently not clear. One possibility is that they are a consequence of the density PDF as stressed in Figure 3. Likely enough strong driving limits the formation of massive collapsing clumps in which a significant fraction of the mass follows a collapse PDF (Equation 10) rather than a lognormal PDF (Equation 7).

### 5.5. Radiative transfer and protostellar heating

As stressed in Section 3.7, the radiation that emanates from the protostars leads to substantial heating of the collapsing envelope and it must be accounted for to properly handle the formation of new fragments. Moreover, the FHSC itself forms because the dust becomes opaque to its own radiation (see Section 3.1.2) and a self-consistent treatment at scale below few AU requires to perform radiative transfer. Several calculations have been performed to study the IMF with self-consistent radiative transfer. Urban et al. (2010) have performed SPH calculations of a  $670 M_{\odot}$  clumps. They introduce sink particles at a density of about  $10^8 \text{ cm}^{-3}$ , and add radiative feedback onto the sink particles. They found that calculations which treat radiative feedback are markedly different from the isothermal ones. The number of stars is reduced by more than an order of magnitude and the stars are consistently more massive when radiation is considered.

Bate (2009) and Bate (2012) carried out high resolution SPH calculations introducing the sink particles at very high density, i.e.  $n > 10^{19} \text{ cm}^{-3}$ . In the simulations no stellar feedback is further added onto the sink particles. The resulting IMF presents a peak at about  $0.3 M_{\odot}$  and a powerlaw mass spectrum at high mass.

Krumholz et al. (2012) carried out AMR calculations with a numerical resolution of 20-40 AU. The sink particles are created when the Jeans length is not resolved any more and only objects more massive than  $0.05 M_{\odot}$  are being considered. Smaller objects are allowed to merge. Both intrinsic and accretion luminosity are added to the sinks as well as fast winds, which are also introduced in some of the calculations. The resulting mass spectra are nearly flat, that is to say  $\Gamma_{IMF} \simeq 0$ , when winds are not considered whereas when winds are added, the radiation can escape along the cavities opened by the winds. In these circumstances, the mass spectra present a peak around  $0.3 M_{\odot}$  and a powerlaw,  $dN/d\log M \propto M^{\Gamma_{IMF}}$ , with  $\Gamma_{IMF} \simeq -0.5$  to -1.

Hennebelle et al. (2020) conducted hydrodynamical AMR simulations of  $1000 M_{\odot}$  clumps with a spatial resolution of 4 to 1 AU. Stellar and accretion luminosities are both included and various efficiencies,  $f_{acc}$  (see Equation 27), ranging from 0 to 50% have been considered. Two sets of initial conditions corresponding to an initial radius of about 0.1



and 0.4 pc have been explored. For the most compact clumps and when  $f_{acc}$  is high, a flat mass spectrum is formed. Otherwise in all runs mass spectra that present a peak around 0.3-0.5  $M_{\odot}$  and a power law at higher masses appear. This is the case even when no radiative feedback applies, i.e. when  $f_{acc} = 0$ . This is also the case when radiation is entirely neglected and that a barotropic equation of state is used. High efficiency radiative feedback runs however tend to present a broader distribution, both at the low mass and high mass end. The most massive stars are up to two to three times more massive than in the barotropic and low-feedback efficiency runs. [Hennebelle et al. \(2022\)](#) have performed MHD runs with a spatial resolution down to 1 AU and which also take into account ambipolar diffusion. As previous authors ([Commerçon et al. 2011](#); [Myers et al. 2013](#)), it has been found that magnetic field and radiation reduce fragmentation, particularly when they are both included. As a result, strong magnetic field and high radiation efficiency models, present top-heavier IMF. A comparison with the analytical model discussed in Section 4.1.4 is presented and it has been concluded that the various IMF inferred can be satisfactorily reproduced (down to objects of masses 0.1-0.2  $M_{\odot}$ ) once the mean sound speed and the mean Alfvén speed are used in the analytical model.

As a general conclusion, there is a consensus amongst the various studies that radiative feedback is playing a significant role regarding the stellar mass spectra that form in relatively dense and massive clouds, likely cluster progenitors. Radiative feedback tends to reduce the number of objects promoting the formation of massive stars and in some circumstances (compact and/or highly magnetized clouds) to even top-heavy IMF. In the context of the gravo-turbulent model discussed in Section 4.1.4 and the thermally dominated regime where  $\Gamma_{IMF} = 0$  (see figure 3), clearly the presence of intense radiative stellar feedback would favor this mode and may explain why a flat IMF is often found in simulations that include radiative stellar feedback.

However the origin of the peak of the IMF itself remains debated. In the works where the FHSC is resolved, the peak seems to be a consequence of the dust opacity and the existence of the FHSC rather than to the heating of the protostars. This is the case in the simulations presented in [Lee & Hennebelle \(2018b\)](#), [Colman & Teyssier \(2020\)](#), [Hennebelle et al. \(2020\)](#) and [Hennebelle et al. \(2022\)](#). This is also likely the case in the studies presented by [Bate \(2009\)](#), [Bate \(2012\)](#) and [Bate \(2019\)](#) where no stellar feedback is being explicitly added and where the FHSC is very nicely described by introducing the sink particles only when the second collapse has started. It is nevertheless important to caution here that whereas numerical convergence has been convincingly established when an hard eos is being used, establishing convergence when radiative transfer is properly accounted for appears to be far more difficult ([Hennebelle et al. 2020](#)) and remains a challenge.

In the work where the FHSC is not resolved, it is claimed that the origin of the peak has to be attributed to stellar radiative feedback (see Section 4.2.2). Detailed analysis performed by [Krumholz et al. \(2016\)](#); [Cunningham et al. \(2018\)](#) have found agreements with the picture proposed in [Krumholz \(2011\)](#) where radiation sets the peak. We stress here that the issues regarding numerical convergence and sink algorithms may be particularly critical and should be thoroughly investigated. Finally we note that the simulations presented in [Hennebelle et al. \(2020\)](#), do not support the validity of the radiative feedback setting the IMF's peak since in these simulations, the peak is found to remain at the same mass even when the accretion luminosity vanishes.

## 5.6. The influence of metallicity

As discussed in Section 3.1, the abundance of heavy elements and of dust (and their *relative* ratios, Sharda et al. 2023) are key quantities regarding the thermal balance of the gas. Since the gas metallicity can vary significantly, typically from  $Z_d = 0.01$  to  $Z_d = 3$  in observed galaxies, investigating the dependence of the IMF on this parameter is important.

In Figure 6 we plot the results from a selection of different recent numerical IMF studies that surveyed metallicity. In  $z \sim 0$  conditions, some initial metallicity studies were performed by Myers et al. (2011) and Bate (2014), studying the collapse and fragmentation of several  $100M_\odot$  for a wide range of metallicity. Both works found that the IMF was remarkably insensitive to metallicity, a result later reproduced by (Bate 2019) and Tanvir & Krumholz (2023) with the same respective codes but with various improvements and additional physics. This agreement is despite large differences in the respective methodologies: with Bate (2014) neglecting radiation from the protostellar surface but resolving  $\lesssim 1$  AU scales and the FHSC, and Myers et al. (2011) accounting for protostellar radiation fully but reaching a maximum resolution of 7AU.

This insensitivity to metallicity is not always found: Guszejnov et al. (2022) found that reducing metallicity increased the mean stellar mass, due to the resulting increased temperature (§3.1). Here the initial conditions and cloud density could be important: their fiducial cloud had a mean density of  $\sim 10^3 \text{ cm}^{-3}$ , where the temperature structure was determined largely by processes *other* than dust cooling, unlike the denser ( $\gtrsim 10^5 \text{ cm}^{-3}$ ) clouds simulated by the above authors. Chon et al. (2022) found an opposite trend: in their simulations reducing metallicity *decreased* the typical stellar mass, while also enabling the formation of a few very-massive stars. Unlike the other works mentioned in this section, they did not account for any radiation other than the CMB, so by neglecting protostellar radiation it is possible that they overestimated disk fragmentation (c.f. Offner et al. 2009).

There is some interplay between the effect of metallicity variations and the background radiation field, e.g. the CMB. Surviving  $z = 0 - 20$ , Chon et al. (2022) reported generally increasing stellar mass with increasing  $z$ . (Bate 2023) found that in a  $z = 5$  CMB their results were essentially the same as those at  $z = 0$  in Bate (2019), except for their  $Z_d = 1$   $z = 5$  model, which was shifted upward by a factor of  $\sim 3$  in mass. This result is in reasonable agreement with the scaling with  $Z_d$  and the radiation field  $u_{\text{rad}} \propto (1+z)^4$  predicted by Equation 6, assuming that the FHSC mass is setting the overall IMF mass scale.

The effect of metallicity on the formation of massive stars and the upper tail or cutoff of the IMF is nuanced, due to several competing effects. As mentioned above, the higher temperatures expected at low metallicity should suppress fragmentation in at least some cases. Lower- $Z$  stars have weaker stellar winds, and dust-poor environments are less subject to the effects of radiation pressure which could regulate massive stellar growth and disrupt the natal clumps. All of these factors would facilitate the formation of very-massive stars. However, the absence of significant metal line cooling in metal-poor HII regions can make them a factor of  $\sim 2$  warmer ( $\sim 20,000\text{K}$ ) than at Solar metallicity. This greatly reduces the ionizing flux, and hence stellar mass, required to create an expanding HII region that can disrupt a star-forming GMC, with  $\mathcal{Q} \propto T^{-2.85}$  (Grudić et al. 2023). This is why the  $0.01Z_\odot$  cloud in Guszejnov et al. (2022) had a significantly reduced star formation efficiency and maximum stellar mass compared to the fiducial case,  $\sim 25M_\odot$  versus  $\sim 45M_\odot$ . Which of the competing feedback scalings sets the upper IMF cutoff is likely to depend on initial conditions, because photoionizing feedback becomes irrelevant compared to radiation

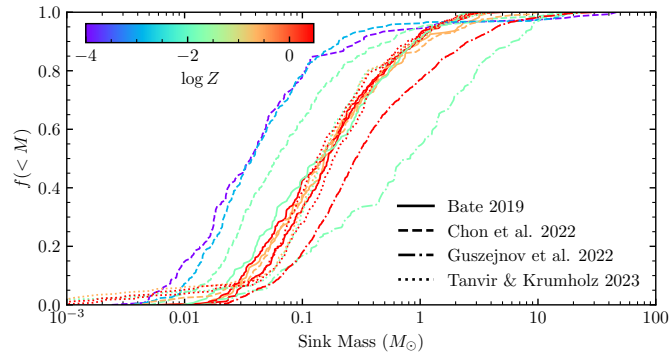


**Figure 6**

Cumulative sink-particle mass distributions reported by multiple numerical parameter studies surveying metallicity: [Bate \(2019\)](#), [Chon et al. \(2022\)](#), [Guszejnov et al. \(2022\)](#), and [Tanvir & Krumholz \(2023\)](#). Line styles plot the different studies, and color encodes the Solar-scaled metallicity as indicated in the colorbar. Note the wide range of results at  $Z_d = 0.01$  (green).

pressure at high densities ([Krumholz & Matzner 2009](#)).

### 5.7. The influence of protostellar jets

The influence of protostellar jets on the evolution of clusters and more specifically on the IMF has been studied by various groups, and several effects have been claimed. First, jets certainly contribute to inject kinetic energy into the collapsing clumps and therefore constitute a significant source of turbulence although the exact amount remains a bit uncertain due to the inaccuracies with which jets properties are hampered (e.g. [Cunningham et al. 2009](#); [Guszejnov et al. 2021](#)) as illustrated in figure 7.

Second, jets limit the star formation rate within star forming regions and lead to values that are in much better agreement with observations than simulations without jets (e.g. [Wang et al. 2010](#); [Federrath 2015](#); [Verliat et al. 2022](#)).

Third, jets appear to shift the peak of the IMF and the mass of the smallest objects which form compared to when they are not included by a factor of several. This effect has been consistently reported in several studies ([Li et al. 2010](#); [Guszejnov et al. 2021](#); [Mathew & Federrath 2021](#)). It is generally admitted that the reason is due to the generation of smaller mass gravitationally unstable density fluctuations induced by the jets. This could also be due to less efficient accretion from the individual mass reservoir, say the cores, due to the jet feedback. The two explanations are not exclusive from each other and may operate simultaneously. Indeed the effect observed on figure 6 of [Guszejnov et al. \(2021\)](#) indicate a substantial shift in the IMF's peak by almost a factor of 10. Note that this may solve a possibly important problem. As discussed previously, several authors ([Lee & Hennebelle 2018a](#); [Jones & Bate 2018](#); [Guszejnov et al. 2020](#)) found that if the thermal support of the star forming clump is too high, a plateau IMF, i.e.  $\Gamma_{IMF} \simeq 0$ , tends to develop. However the clump initial density values at which this happens are not particularly low compared to observations and therefore, jets likely constitute a solution by regulating kinetic energy in collapsing clumps. Let us stress a possible caveat. In most of works which so far have been investigating the impact of jets, the FHSC is actually not resolved and therefore

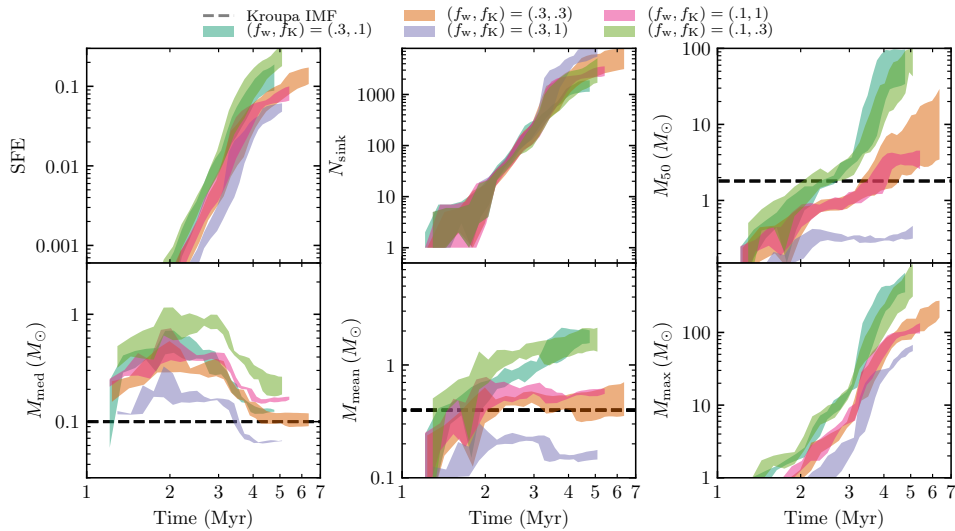


**Figure 7**

Result of a parameter study of  $2 \times 10^4 M_\odot$  GMC simulations with protostellar jet feedback, varying only the feedback parameters  $f_w$  and  $f_K$  (Guszejnov et al. 2021). Plotted as a function of time are the fraction of gas mass converted to stars (SFE), the number of sink particles ( $N_{\text{sink}}$ ), the mass-weighted median stellar mass  $M_{50}$ , median and mean sink mass  $M_{\text{med}}$  and  $M_{\text{mean}}$ , and the maximum sink mass  $M_{\text{max}}$ . Note the large overlap of  $N_{\text{sink}}$  versus time for all models; the strength of jet feedback does not fundamentally affect fragmentation physics. Also note the correspondance between models with similar values of the jet momentum loading  $f_w f_K$ , indicating that jet feedback operates in a momentum-driven regime.

fragmentation is limited by numerical resolution. Very recently Lebreuilly et al. (2023a) have performed the first simulations with jets and about 1 AU resolution. They found that whereas jets do not affect the number of objects with mass below or comparable to a few times the mass of the FHSC, they indeed reduce the mean object mass in the simulation.

Finally, jets may also be playing an important role regarding stellar radiation feedback since they open up cavities along which photons may escape but also because they reduce the accretion rate onto the stars, both effects concur to diminish the effective radiation feedback that the collapsing clump is experiencing (e.g. Hansen et al. 2012). These effects, which add up to the ones discussed above, are clearly present in the simulations presented for instance in figure 8 of Krumholz et al. (2012) where the simulation without wind exhibits a clear plateau ( $\Gamma_{\text{IMF}} = 0$ ) whereas the ones with wind present a clear powerlaw with  $\Gamma_{\text{IMF}} \gtrsim -1$ .

### 5.8. Massive stellar feedback and cloud disruption

It is generally agreed that winds and radiation from massive stars are the key processes regulating star formation on the scale of giant molecular clouds and ultimately dispersing them (Section 3.7.2 and 3.7.3). This directly affects the gas supply for accretion and fragmentation, and the dynamics of star cluster assembly and dispersal, all of which affect the IMF. The mass spectra predicted by calculations neglecting these processes are literally

inconclusive, because the stellar masses must be extracted at some arbitrary time or final SFE, and further evolution of the mass spectrum cannot be ruled out. The usual choice of a constant  $\sim 5 - 20\%$  SFE is probably accurate in detail, because cloud-scale calculations with feedback unanimously find that SFE varies with cloud/clump properties, most notably surface density (Chevance et al. 2023).

Massive stellar winds/radiation and cloud disruption have only recently begun to be accounted for in star cluster formation simulations intended to model the IMF. Gavagnin et al. (2017) and He et al. (2019) both performed RHD star cluster formation simulations with sink particles emitting ionizing radiation and no other feedback, and both found a flat and/or top-heavy mass spectrum incompatible with the observed IMF, suggesting that photoionization alone is not sufficient to regulate the entire IMF, although it can regulate the high-mass regime. But in the past year, the first studies accounting for winds and/or radiation in concert with protostellar outflows have emerged (Verliat et al. 2022; Grudić et al. 2022). The STARFORGE studies have demonstrated the complementary roles of different feedback processes in setting the IMF: protostellar jets have a dominant effect on the  $\sim 0.1 - 1M_{\odot}$  range, but cannot disrupt  $\gtrsim 10^4 M_{\odot}$  clouds or regulate runaway accretion of the most massive stars (Guszejnov et al. 2021). Accretion onto the most-massive stars continues via filamentary,  $\sim 1 - 10\text{pc}$  scale flows until halted by feedback; this tends to coincide with the disruption of the cloud as a whole (Guszejnov et al. 2022). Until the cloud is disrupted and star formation is quenched, the stellar mass spectrum evolves continuously. This mode of self-regulated massive star formation inevitably results in a maximum stellar mass that depends on the cloud bulk properties and composition (Grudić et al. 2023). This sensitivity to initial conditions highlights the importance of characterizing the initial conditions for star formation further, and exploring simulation setups that are more realistic than the usual idealized periodic box or isolated clump setups.

#### SUMMARY POINTS

1. Tremendous progresses have been accomplished during the last two decades in our understanding of the IMF. It is now possible to self-consistently treat most of the physical processes thought to play a role in setting up the IMF and to better cover the necessary large range of spatial scales, from pc to AU, though further lines of necessary improvements remain.
2. Self-gravity, turbulence, and feedback are responsible for setting the stellar mass spectrum for masses above few  $M_{\odot}$ . Gravo-turbulent theories as well as competitive accretion make specific predictions for the powerlaw exponent of the IMF,  $\Gamma_{IMF}$ , which depending on the physical conditions is predicted to be equal to 0,  $-3/4$ ,  $-1$  or  $\simeq -1.3$ . Whereas these different regimes may be relatively universal, the stellar masses for which they apply depend on large scale environments such as magnetic field, Mach number and temperature.  $\Gamma_{IMF} = 0$  is predicted to develop in collapsing clouds in which thermal and magnetic supports dominate over turbulence.
3. Protostellar jets, by injecting kinetic energy in star forming clumps, may limit powerlaw exponent  $\Gamma_{IMF} = 0$  and favor  $\Gamma_{IMF} = -3/4$  to  $-1$ .
4. By significantly increasing the temperature of the star forming clumps favor the formation of massive stars, radiative stellar feedback, depending of the circumstances, may favor the development of a powerlaw exponent  $\Gamma_{IMF} = 0$  for stellar masses up to a few  $M_{\odot}$ . Strong magnetic fields are expected to produce similar effects.

5. The characteristic mass of stars, that is to say, the peak of the IMF, is likely, at least in some circumstances, a consequence of the first hydrostatic core around which tidal forces reduce fragmentation allowing further accretion.
6. The influence of numerical resolution and of the sink particle algorithms may have drastic consequences on the computed IMF and their influences should be carefully verified. This is particularly critical for the characteristic mass or peak of the IMF.

### FUTURE ISSUES

1. The links between CMF and IMF should be further investigated. This requests a thorough definition and distinction between an observed *core* and an effective *reservoir*, that is to say the gas mass that is eventually accreted by a star. The statistics of the *core* and the *reservoir* should then be compared.
2. An important issue for future simulations will be to improve spatial resolution and systematically check for numerical convergence. In particular, describing well the first hydrostatic core and making sure that the results are independent of sink particle algorithms is crucial.
3. It is fundamental to improve statistics by performing simulations of more massive clumps and by running series of independent realisations of similar initial conditions but also to systematically explore the dependence of the IMF on a large variety of initial conditions. The spatial resolution of these simulations must be sufficient to resolve AU scales and produce low mass objects whereas the largest spatial scale should be sufficient to form the most massive stars.
4. It is necessary to keep developing analytical modeling and to perform comparisons with simulation results. This is the only way to obtain generic results and to understand the physical processes.
5. The physics that is being treated should be further improved. This is particularly the case for dust, radiative transfer and non-ideal MHD. Presently, the opacities and the resistivities still suffer large uncertainties. Let us stress also that whereas carrying out more and more realistic simulations is obviously an important goal, intentionally-simplified models are also necessary to understand the physical processes.
6. A key achievement will be detailed and complete modeling of well observationally constrained specific regions both for the gas and the stellar populations.

### DISCLOSURE STATEMENT

The authors are not aware of any affiliations, memberships, funding, or financial holdings that might be perceived as affecting the objectivity of this review.

### ACKNOWLEDGMENTS

We are grateful to Lynne Hillenbrand for making available her compilation of IMF measurements, Sunmyon Chon and Tab Tanvir for sharing their simulation IMF data, and

to Matthew Bate, Mark Krumholz, Philippe André, Gilles Chabrier, Shu-ichiro Inutsuka, Yueh-Ning Lee and Frédérique Motte for helpful discussions. We thank Estelle Moraux and Ugo Lebreuilly for a critical reading of the manuscript and David Guszejnov for extended discussions about this review. We are very grateful to Eve Ostriker for a detailed reading of the manuscript and numerous constructive comments which led to significant improvements. This research has received funding from the European Research Council synergy grant ECOGAL (Grant : 855130). Support for MYG was provided by NASA through the NASA Hubble Fellowship grant #HST-HF2-51479 awarded by the Space Telescope Science Institute, which is operated by the Association of Universities for Research in Astronomy, Inc., for NASA, under contract NAS5-26555.

## LITERATURE CITED

- André P, Men'shchikov A, Bontemps S, Könyves V, Motte F, et al. 2010. *A&A* 518:L102
- Bakes ELO, Tielens AGGM. 1994. *ApJ* 427:822
- Ballesteros-Paredes J. 2006. *MNRAS* 372(1):443–449
- Ballesteros-Paredes J, Hartmann LW, Pérez-Goytia N, Kuznetsova A. 2015. *MNRAS* 452:566–574
- Bally J. 2016. *ARA&A* 54:491–528
- Banerjee S, Kroupa P. 2012. *A&A* 547:A23
- Bartko H, Martins F, Trippe S, Fritz TK, Genzel R, et al. 2010. *ApJ* 708(1):834–840
- Bastian N, Covey KR, Meyer MR. 2010. *ARA&A* 48:339–389
- Basu S. 2000. *ApJL* 540(2):L103–L106
- Basu S, Gil M, Auddy S. 2015. *MNRAS* 449(3):2413–2420
- Basu S, Jones CE. 2004. *MNRAS* 347(3):L47–L51
- Bate MR. 2009. *MNRAS* 392(4):1363–1380
- Bate MR. 2012. *MNRAS* 419(4):3115–3146
- Bate MR. 2014. *MNRAS* 442:285–313
- Bate MR. 2019. *MNRAS* 484(2):2341–2361
- Bate MR. 2023. *MNRAS* 519(1):688–708
- Bate MR, Bonnell IA. 2005. *MNRAS* 356:1201–1221
- Bate MR, Bonnell IA, Bromm V. 2003. *MNRAS* 339:577–599
- Bate MR, Bonnell IA, Price NM. 1995. *MNRAS* 277:362–376
- Bate MR, Burkert A. 1997. *MNRAS* 288(4):1060–1072
- Baumgardt H, Hénault-Brunet V, Dickson N, Sollima A. 2023. *MNRAS* 521(3):3991–4008
- Baumgardt H, Sollima S. 2017. *MNRAS* 472(1):744–750
- Bialy S, Sternberg A. 2019. *ApJ* 881(2):160
- Binney J, Tremaine S. 2008. *Galactic Dynamics: Second Edition*
- Black DC, Bodenheimer P. 1975. *ApJ* 199:619–632
- Blandford RD, Payne DG. 1982. *MNRAS* 199:883–903
- Bleuler A, Teyssier R. 2014. *MNRAS* 445(4):4015–4036
- Bonazzola S, Heyvaerts J, Falgarone E, Perault M, Puget JL. 1987. *A&A* 172(1-2):293–298
- Bonnell IA, Clark P, Bate MR. 2008. *MNRAS* 389(4):1556–1562
- Bonnell IA, Clarke CJ, Bate MR. 2006. *MNRAS* 368(3):1296–1300
- Bonnell IA, Clarke CJ, Bate MR, Pringle JE. 2001. *MNRAS* 324(3):573–579
- Bonnell IA, Larson RB, Zinnecker H. 2007. *The Origin of the Initial Mass Function. In Protostars and Planets V*, eds. B Reipurth, D Jewitt, K Keil
- Bonnell IA, Smith RJ, Clark PC, Bate MR. 2011. *MNRAS* 410(4):2339–2346
- Bonnor WB. 1956. *MNRAS* 116:351
- Castaing B. 1996. *Journal de Physique II* 6(1):105–114
- Chabrier G. 2003. *PASP* 115:763–795

- Chabrier G. 2005. *The Initial Mass Function: from Salpeter 1955 to 2005*. In *The Initial Mass Function 50 Years Later*, eds. E Corbelli, F Palla, H Zinnecker, vol. 327 of *Astrophysics and Space Science Library*
- Chabrier G, Hennebelle P, Charlot S. 2014. *ApJ* 796(2):75
- Chabrier G, Lenoble R. 2023. *arXiv e-prints* :arXiv:2301.05139
- Chakrabarti S, McKee CF. 2008. *ApJ* 683(2):693–706
- Chevance M, Krumholz MR, McLeod AF, Ostriker EC, Rosolowsky EW, Sternberg A. 2023. *The Life and Times of Giant Molecular Clouds*. In *Protostars and Planets VII*, eds. S Inutsuka, Y Aikawa, T Muto, K Tomida, M Tamura, vol. 534 of *Astronomical Society of the Pacific Conference Series*
- Chon S, Ono H, Omukai K, Schneider R. 2022. *MNRAS* 514(3):4639–4654
- Colman T, Teyssier R. 2020. *MNRAS* 492(4):4727–4751
- Commerçon B, Hennebelle P, Henning T. 2011. *ApJL* 742:L9
- Commerçon B, Hennebelle P, Audit E, Chabrier G, Teyssier R. 2008. *A&A* 482(1):371–385
- Commerçon B, Teyssier R, Audit E, Hennebelle P, Chabrier G. 2011. *A&A* 529:A35
- Crutcher RM. 2012. *ARA&A* 50:29–63
- Cunningham AJ, Frank A, Carroll J, Blackman EG, Quillen AC. 2009. *ApJ* 692(1):816–826
- Cunningham AJ, Klein RI, Krumholz MR, McKee CF. 2011. *ApJ* 740:107
- Cunningham AJ, Krumholz MR, McKee CF, Klein RI. 2018. *MNRAS* 476:771–792
- Da Rio N, Robberto M, Hillenbrand LA, Henning T, Stassun KG. 2012. *ApJ* 748(1):14
- Dale JE, Ngoumou J, Ercolano B, Bonnell IA. 2013. *MNRAS* 436(4):3430–3445
- Dib S. 2014. *MNRAS* 444(2):1957–1981
- Dib S, Kim J, Shadmehri M. 2007. *MNRAS* 381(1):L40–L44
- Dib S, Shadmehri M, Padoan P, Maheswar G, Ojha DK, Khajenabi F. 2010. *MNRAS* 405(1):401–420
- Draine BT. 2011. *Physics of the Interstellar and Intergalactic Medium*
- Ebrahimi H, Sollima A, Haghi H, Baumgardt H, Hilker M. 2020. *MNRAS* 494(3):4226–4243
- Edgar R. 2004. *New Astron. Rev.* 48(10):843–859
- Elmegreen BG, Klessen RS, Wilson CD. 2008. *ApJ* 681(1):365–374
- Elmegreen BG, Mathieu RD. 1983. *MNRAS* 203:305–315
- Elmegreen BG, Scalo J. 2004. *ARA&A* 42:211–273
- Federrath C. 2013. *MNRAS* 436:1245–1257
- Federrath C. 2015. *MNRAS* 450(4):4035–4042
- Federrath C, Klessen RS, Schmidt W. 2008. *ApJL* 688:L79
- Federrath C, Roman-Duval J, Klessen RS, Schmidt W, Mac Low MM. 2010. *A&A* 512:A81
- Federrath C, Schrön M, Banerjee R, Klessen RS. 2014. *ApJ* 790:128
- Foster PN, Chevalier RA. 1993. *ApJ* 416:303
- Gavagnin E, Bleuler A, Rosdahl J, Teyssier R. 2017. *MNRAS* 472(4):4155–4172
- Geen S, Hennebelle P, Tremblin P, Rosdahl J. 2016. *MNRAS* 463(3):3129–3142
- Gerrard IA, Federrath C, Kuruwita R. 2019. *MNRAS* 485(4):5532–5542
- Girichidis P, Federrath C, Banerjee R, Klessen RS. 2011. *MNRAS* 413(4):2741–2759
- Girichidis P, Offner SSR, Kritsuk AG, Klessen RS, Hennebelle P, et al. 2020. *Space Sci. Rev.* 216(4):68
- Glover SCO, Abel T. 2008. *MNRAS* 388(4):1627–1651
- Glover SCO, Clark PC. 2012. *MNRAS* 421(1):9–19
- Glover SCO, Jappsen AK. 2007. *ApJ* 666(1):1–19
- Goldsmith PF. 2001. *ApJ* 557(2):736–746
- Gong M, Ostriker EC. 2015. *ApJ* 806:31
- Gong M, Ostriker EC, Wolfire MG. 2017. *ApJ* 843(1):38
- Grudić MY, Hopkins PF, Lee EJ, Murray N, et al. 2019. *MNRAS* 488(2):1501–1518
- Grudić MY, Guszejnov D, Hopkins PF, Offner SSR, Faucher-Giguère CA. 2021. *MNRAS*



- 506(2):2199–2231
- Grudić MY, Guszejnov D, Offner SSR, Rosen AL, Raju AN, et al. 2022. *MNRAS* 512(1):216–232
- Grudić MY, Hopkins PF. 2023. *arXiv e-prints* :arXiv:2308.16268
- Grudić MY, Offner SSR, Guszejnov D, Faucher-Giguère CA, Hopkins PF. 2023. *arXiv e-prints* :arXiv:2307.00052
- Gu M, Greene JE, Newman AB, Kreisch C, Quenneville ME, et al. 2022. *ApJ* 932(2):103
- Guerrero-Gamboa R, Vázquez-Semadeni E. 2020. *ApJ* 903(2):136
- Guillet V, Hennebelle P, Pineau des Forêts G, Marcowith A, Commerçon B, Marchand P. 2020. *A&A* 643:A17
- Guszejnov D, Grudić MY, Hopkins PF, Offner SSR, Faucher-Giguère CA. 2020. *MNRAS* 496(4):5072–5088
- Guszejnov D, Grudić MY, Hopkins PF, Offner SSR, Faucher-Giguère CA. 2021. *MNRAS* 502(3):3646–3663
- Guszejnov D, Grudić MY, Offner SSR, Faucher-Giguère CA, Hopkins PF, Rosen AL. 2022. *MNRAS* 515(4):4929–4952
- Guszejnov D, Hopkins PF, Grudić MY, Krumholz MR, Federrath C. 2018. *MNRAS* 480:182–191
- Guszejnov D, Krumholz MR, Hopkins PF. 2016. *MNRAS* 458:673–680
- Hacar A, Clark SE, Heitsch F, Kainulainen J, Panopoulou GV, et al. 2023. 534:153
- Hansen CE, Klein RI, McKee CF, Fisher RT. 2012. *ApJ* 747:22
- Haugbølle T, Padoan P, Nordlund Å. 2018. *ApJ* 854(1):35
- He CC, Ricotti M, Geen S. 2019. *MNRAS* 489(2):1880–1898
- Heger A, Müller B, Mandel I. 2023. *arXiv e-prints* :arXiv:2304.09350
- Hennebelle P. 2021. *A&A* 655:A3
- Hennebelle P, Chabrier G. 2008. *ApJ* 684:395–410
- Hennebelle P, Chabrier G. 2009. *ApJ* 702:1428–1442
- Hennebelle P, Commerçon B, Lee YN, Chabrier G. 2020. *ApJ* 904(2):194
- Hennebelle P, Falgarone E. 2012. *A&A* 20:55
- Hennebelle P, Inutsuka Si. 2019. *Frontiers in Astronomy and Space Sciences* 6:5
- Hennebelle P, Lebreuilly U, Colman T, Elia D, Fuller G, et al. 2022. *A&A* 668:A147
- Hennebelle P, Lee YN, Chabrier G. 2019. *ApJ* 883(2):140
- Hillenbrand LA. 2004. *The Mass Function of Newly Formed Stars*. In *The Dense Interstellar Medium in Galaxies*, eds. S Pfalzner, C Kramer, C Staubmeier, A Heithausen, vol. 91
- Hollenbach D, McKee CF. 1979. *ApJS* 41:555–592
- Hollyhead K, Bastian N, Adamo A, Silva-Villa E, Dale J, et al. 2015. *MNRAS* 449(1):1106–1117
- Hopkins AM. 2018. *PASA* 35:e039
- Hopkins PF. 2012a. *MNRAS* 423:2016–2036
- Hopkins PF. 2012b. *MNRAS* 423:2037–2044
- Hopkins PF. 2013a. *MNRAS* 430:1880–1891
- Hopkins PF. 2013b. *MNRAS* 433(1):170–177
- Hosek Matthew W. J, Lu JR, Anderson J, Najarro F, Ghez AM, et al. 2019. *ApJ* 870(1):44
- Hosokawa T, Omukai K. 2009. *ApJ* 691(1):823–846
- Hoyle F. 1953. *ApJ* 118:513
- Hsu WH, Hartmann L, Heitsch F, Gómez GC. 2010. *ApJ* 721(2):1531–1546
- Hubber DA, Walch S, Whitworth AP. 2013. *MNRAS* 430(4):3261–3275
- Indriolo N, McCall BJ. 2012. *ApJ* 745(1):91
- Inutsuka Si. 2001. *ApJ* 559(2):L149–L152
- Inutsuka SI, Miyama SM. 1992. *ApJ* 388:392–399
- Jappsen AK, Klessen RS, Larson RB, Li Y, Mac Low MM. 2005. *A&A* 435:611–623
- Jeans JH. 1902. *Philosophical Transactions of the Royal Society of London Series A* 199:1–53
- Jones MO, Bate MR. 2018. *MNRAS* 478(2):2650–2662
- Kim JG, Gong M, Kim CG, Ostriker EC. 2023. *ApJS* 264(1):10

- Kim JG, Kim WT, Ostriker EC. 2016. *ApJ* 819(2):137
- Kirkpatrick JD, Gelino CR, Faherty JK, Meisner AM, Caselden D, et al. 2021. *ApJS* 253(1):7
- Klessen RS. 2001. *ApJ* 556(2):837–846
- Klessen RS, Glover SCO. 2023. *arXiv e-prints* :arXiv:2303.12500
- Kolmogorov A. 1941. *Akademiia Nauk SSSR Doklady* 30:301–305
- Könyves V, André P, Men'shchikov A, Palmeirim P, Arzoumanian D, et al. 2015. *A&A* 584:A91
- Kratter KM, Matzner CD, Krumholz MR, Klein RI. 2010. *ApJ* 708:1585–1597 Reference to disk fragmentation stability. Xicrit is a few.
- Kritsuk AG, Norman ML, Padoan P, Wagner R. 2007. *ApJ* 665(1):416–431
- Kritsuk AG, Norman ML, Wagner R. 2011. *ApJL* 727:L20
- Kroupa P. 2002. *Science* 295:82–91
- Kroupa P, Weidner C, Pflamm-Altenburg J, Thies I, Dabringhausen J, et al. 2013. *The Stellar and Sub-Stellar Initial Mass Function of Simple and Composite Populations*. In *Planets, Stars and Stellar Systems. Volume 5: Galactic Structure and Stellar Populations*, eds. TD Oswalt, G Gilmore, vol. 5. 115
- Krumholz MR. 2011. *ApJ* 743:110
- Krumholz MR. 2014. *Physics Reports* 539:49–134
- Krumholz MR. 2015. *arXiv e-prints* :arXiv:1511.03457
- Krumholz MR, Federrath C. 2019. *arXiv e-prints*
- Krumholz MR, Klein RI, McKee CF. 2012. *ApJ* 754(1):71
- Krumholz MR, Klein RI, McKee CF, Offner SSR, Cunningham AJ. 2009. *Science* 323(5915):754
- Krumholz MR, Leroy AK, McKee CF. 2011. *ApJ* 731(1):25
- Krumholz MR, Matzner CD. 2009. *ApJ* 703(2):1352–1362
- Krumholz MR, McKee CF, Klein RI. 2004. *ApJ* 611:399–412
- Krumholz MR, McKee CF, Klein RI. 2006. *ApJ* 638(1):369–381
- Krumholz MR, Myers AT, Klein RI, McKee CF. 2016. *MNRAS* 460:3272–3283
- Kuiper R, Klahr H, Beuther H, Henning T. 2010. *ApJ* 722(2):1556–1576
- Kuznetsova A, Hartmann L, Burkert A. 2017. *ApJ* 836(2):190
- Kuznetsova A, Hartmann L, Heitsch F, Ballesteros-Paredes J. 2018. *ApJ* 868(1):50
- Lamers HJGLM, Snow TP, Lindholm DM. 1995. *ApJ* 455:269
- Larson RB. 1969. *MNRAS* 145:271
- Larson RB. 1973. *MNRAS* 161:133
- Larson RB. 1981. *MNRAS* 194:809–826
- Larson RB. 2005. *MNRAS* 359(1):211–222
- Larson RB, Starrfield S. 1971. *A&A* 13:190
- Lebreuilly U, Hennebelle P, Colman T, Commerçon B, Klessen R, et al. 2021. *ApJL* 917(1):L10
- Lebreuilly U, Hennebelle P, Maury A, González M, Traficante A, et al. 2023a. *arXiv e-prints* :arXiv:2309.05397
- Lebreuilly U, Vallucci-Goy V, Guillet V, Lombart M, Marchand P. 2023b. *MNRAS* 518(3):3326–3343
- Lee AT, Cunningham AJ, McKee CF, Klein RI. 2014. *ApJ* 783(1):50
- Lee YN, Hennebelle P. 2018a. *A&A* 611:A88
- Lee YN, Hennebelle P. 2018b. *A&A* 611:A89
- Lee YN, Hennebelle P. 2019. *A&A* 622:A125
- Lee YN, Hennebelle P, Chabrier G. 2017. *ApJ* 847(2):114
- Lee YN, Offner SSR, Hennebelle P, André P, Zinnecker H, et al. 2020. *Space Sci. Rev.* 216(4):70
- Li J, Liu C, Zhang ZY, Tian H, Fu X, et al. 2023. *Nature* 613(7944):460–462
- Li ZY, Wang P, Abel T, Nakamura F. 2010. *ApJL* 720(1):L26–L30
- Lim B, Chun MY, Sung H, Park BG, Lee JJ, et al. 2013. *AJ* 145(2):46
- Lin CC, Mestel L, Shu FH. 1965. *ApJ* 142:1431
- Louvet F, Hennebelle P, Men'shchikov A, Didelon P, Ntormousi E, Motte F. 2021. *A&A* 653:A157

- Low C, Lynden-Bell D. 1976. *MNRAS* 176:367–390
- Lu JR, Do T, Ghez AM, Morris MR, Yelda S, Matthews K. 2013. *ApJ* 764(2):155
- Lu ZJ, Pelkonen VM, Padoan P, Pan L, Haugbølle T, Nordlund Å. 2020. *ApJ* 904(1):58
- Luhman KL. 2012. *ARA&A* 50:65–106
- Luhman KL. 2018. *AJ* 156(6):271
- Mac Low MM. 1999. *ApJ* 524(1):169–178
- Mac Low MM, Klessen RS. 2004. *Reviews of Modern Physics* 76:125–194
- Martel H, Evans II NJ, Shapiro PR. 2006. *ApJS* 163:122–144
- Maschberger T. 2013a. *MNRAS* 429:1725–1733
- Maschberger T. 2013b. *MNRAS* 436(2):1381–1389
- Maschberger T, Bonnell IA, Clarke CJ, Moraux E. 2014. *MNRAS* 439(1):234–246
- Massey P. 2003. *ARA&A* 41:15–56
- Masunaga H, Inutsuka Si. 2000. *ApJ* 531:350–365
- Masunaga H, Miyama SM, Inutsuka Si. 1998. *ApJ* 495:346–369
- Mathew SS, Federrath C. 2021. *MNRAS* 507(2):2448–2467
- Mathew SS, Federrath C, Seta A. 2023. *MNRAS* 518(4):5190–5214
- Matzner CD, McKee CF. 1999. *ApJL* 526(2):L109–L112
- Maud LT, Moore TJJ, Lumsden SL, Mottram JC, Urquhart JS, Hoare MG. 2015. *MNRAS* 453(1):645–665
- McKee CF, Ostriker EC. 2007. *ARA&A* 45:565–687
- McKee CF, Tan JC. 2003. *ApJ* 585(2):850–871
- Moe M, Di Stefano R. 2016. *ArXiv e-prints*
- Mor R, Robin AC, Figueras F, Roca-Fàbrega S, Luri X. 2019. *A&A* 624:L1
- Motte F, Andre P, Neri R. 1998. *A&A* 336:150–172
- Motte F, Nony T, Louvet F, Marsh KA, Bontemps S, et al. 2018. *ArXiv e-prints*
- Myers AT, Krumholz MR, Klein RI, McKee CF. 2011. *ApJ* 735:49
- Myers AT, McKee CF, Cunningham AJ, Klein RI, Krumholz MR. 2013. *ApJ* 766(2):97
- Myers PC. 2009. *ApJ* 706(2):1341–1352
- Naab T, Ostriker JP. 2017. *ARA&A* 55(1):59–109
- Nakano T, Hasegawa T, Morino JI, Yamashita T. 2000. *ApJ* 534(2):976–983
- Neufeld DA, Wolfire MG. 2017. *ApJ* 845(2):163
- Newman AB, Smith RJ, Conroy C, Villaume A, van Dokkum P. 2017. *ApJ* 845(2):157
- Nordlund ÅK, Padoan P. 1999. *The Density PDFs of Supersonic Random Flows*. In *Interstellar Turbulence*, eds. J Franco, A Carraminana
- Offner SSR, Clark PC, Hennebelle P, Bastian N, Bate MR, et al. 2014. *Protostars and Planets VI* :53–75
- Offner SSR, Klein RI, McKee CF, Krumholz MR. 2009. *ApJ* 703(1):131–149
- Offner SSR, Moe M, Kratter KM, Sadavoy SI, Jensen ELN, Tobin JJ. 2022. *arXiv e-prints* :arXiv:2203.10066
- Osterbrock DE, Ferland GJ. 2006. *Astrophysics of gaseous nebulae and active galactic nuclei*
- Ostriker EC, Kim CG. 2022. *ApJ* 936(2):137
- Padoan P, Nordlund Å. 2002. *ApJ* 576:870–879
- Padoan P, Nordlund A, Jones BJT. 1997. *MNRAS* 288:145–152
- Padoan P, Pelkonen VM, Juvella M, Haugbølle T, Nordlund Å. 2023. *MNRAS* 522(3):3548–3567
- Padovani M. 2023. *On the origin of cosmic-ray ionisation in star-forming regions*. In *Physics and Chemistry of Star Formation: The Dynamical ISM Across Time and Spatial Scales*
- Palla F, Stahler SW. 1991. *ApJ* 375:288
- Pang X, Grebel EK, Allison RJ, Goodwin SP, Altmann M, et al. 2013. *ApJ* 764(1):73
- Parravano A, McKee CF, Hollenbach DJ. 2011. *ApJ* 726(1):27
- Pelkonen VM, Padoan P, Haugbølle T, Nordlund Å. 2021. *MNRAS* 504(1):1219–1236
- Pelletier G, Pudritz RE. 1992. *ApJ* 394:117

- Penston MV. 1969. *MNRAS* 144:425
- Pineda JE, Arzoumanian D, André P, Friesen RK, Zavagno A, et al. 2022. *arXiv e-prints* :arXiv:2205.03935
- Pouteau Y, Motte F, Nony T, Galván-Madrid R, Men'shchikov A, et al. 2022. *arXiv e-prints* :arXiv:2203.03276
- Press WH, Schechter P. 1974. *ApJ* 187:425–438
- Price NM, Podsiadlowski P. 1995. *MNRAS* 273(4):1041–1068
- Rabatin B, Collins DC. 2022. *MNRAS*
- Ray TP, McCaughrean MJ, Caratti o Garatti A, Kavanagh PJ, Justtanont K, et al. 2023. *Nature*
- Rees MJ. 1976. *MNRAS* 176:483–486
- Robertson B, Goldreich P. 2012. *ApJL* 750:L31
- Rogers H, Pittard JM. 2013. *MNRAS* 431(2):1337–1351
- Rosen AL. 2022. *ApJ* 941(2):202
- Rosen AL, Offner SSR, Foley MM, Lopez LA. 2021. *arXiv e-prints* :arXiv:2107.12397
- Ruffert M. 1996. *A&A* 311:817–832
- Salpeter EE. 1955. *ApJ* 121:161
- Saumon D, Chabrier G, van Horn HM. 1995. *ApJS* 99:713
- Scalo J. 1998. *The IMF Revisited: A Case for Variations*. In *The Stellar Initial Mass Function (38th Herstonceux Conference)*, eds. G Gilmore, D Howell, vol. 142 of *Astronomical Society of the Pacific Conference Series*
- Schmidt M. 1963. *ApJ* 137:758
- Schmidt W, Kern SAW, Federrath C, Klessen RS. 2010. *A&A* 516:A25
- Schneider FRN, Sana H, Evans CJ, Bestenlehner JM, Castro N, et al. 2018. *Science* 359(6371):69–71
- Sharda P, Amarsi AM, Grasha K, Krumholz MR, Yong D, et al. 2023. *MNRAS* 518(3):3985–3998
- Sharda P, Krumholz MR. 2022. *MNRAS* 509(2):1959–1984
- Shu FH. 1977. *ApJ* 214:488–497
- Shu FH, Adams FC, Lizano S. 1987. *ARA&A* 25:23–81
- Shu FH, Lizano S, Ruden SP, Najita J. 1988. *ApJL* 328:L19
- Silk J. 1977. *ApJ* 214:152–160
- Silk J. 1995. *ApJL* 438:L41
- Smith RJ. 2020. *ARA&A* 58:577–615
- Smith RJ, Clark PC, Bonnell IA. 2008. *MNRAS* 391(3):1091–1099
- Smith RJ, Clark PC, Bonnell IA. 2009. *MNRAS* 396:830–841
- Smith RJ, Glover SCO, Klessen RS. 2014. *MNRAS* 445:2900–2917
- Sollima A. 2019. *MNRAS* 489(2):2377–2394
- Szécsi D, Agrawal P, Wünsch R, Langer N. 2022. *A&A* 658:A125
- Takemura H, Nakamura F, Arce HG, Schneider N, Ossenkopf-Okada V, et al. 2023. *ApJS* 264(2):35
- Tan JC, Beltrán MT, Caselli P, Fontani F, Fuente A, et al. 2014. *Massive Star Formation*. In *Protostars and Planets VI*, eds. H Beuther, RS Klessen, CP Dullemond, T Henning
- Tanvir TS, Krumholz MR. 2023. *arXiv e-prints* :arXiv:2305.20039
- Teyssier R, Commerçon B. 2019. *Frontiers in Astronomy and Space Sciences* 6:51
- Tielens AGGM. 2005. *The Physics and Chemistry of the Interstellar Medium*
- Tomida K, Tomisaka K, Matsumoto T, Hori Y, Okuzumi S, et al. 2013. *ApJ* 763(1):6
- Truelove JK, Klein RI, McKee CF, Holliman II JH, Howell LH, Greenough JA. 1997. *ApJL* 489:L179–L183
- Urban A, Martel H, Evans Neal J. I. 2010. *ApJ* 710(2):1343–1364
- van Dokkum PG, Conroy C. 2010. *Nature* 468:940–942
- Vaytet N, Haugbølle T. 2017. *A&A* 598:A116
- Vaytet N, Tomida K, Chabrier G. 2014. *A&A* 563:A85
- Vázquez-Semadeni E. 1994. *ApJ* 423:681
- Verliat A, Hennebelle P, González M, Lee YN, Geen S. 2022. *A&A* 663:A6

- Vink JS, de Koter A, Lamers HJGLM. 2001. *A&A* 369:574–588
- Walch S, Naab T. 2015. *MNRAS* 451:2757–2771
- Wang P, Li ZY, Abel T, Nakamura F. 2010. *ApJ* 709:27–41
- Ward-Thompson D, André P, Crutcher R, Johnstone D, Onishi T, Wilson C. 2007. *Protostars and Planets V* :33–46
- Wegg C, Gerhard O, Portail M. 2017. *ApJL* 843(1):L5
- Weingartner JC, Draine BT. 2001. *ApJS* 134(2):263–281
- Weisz DR, Fouesneau M, Hogg DW, Rix HW, Dolphin AE, et al. 2013. *ApJ* 762(2):123
- Weisz DR, Johnson LC, Foreman-Mackey D, Dolphin AE, Beerman LC, et al. 2015. *ApJ* 806:198
- Whitworth AP, Jaffa SE. 2018. *A&A* 611:A20
- Wiesenfeld L, Goldsmith PF. 2014. *ApJ* 780(2):183
- Zentner AR. 2007. *International Journal of Modern Physics D* 16(5):763–815
- Zhao B, Tomida K, Hennebelle P, Tobin JJ, Maury A, et al. 2020. *Space Sci. Rev.* 216(3):43
- Zinnecker H. 1982. *Annals of the New York Academy of Sciences* 395:226–235
- Zinnecker H. 1984. *MNRAS* 210:43–56